工學博士學位論文

Fabrication of exfoliated graphene nanomaterials from graphite and their applications

흑연으로부터 박리된 그래핀 나노재료의 제조와 응용

2013年 2月

서울大學校 大學院

化學生物工學部

閔 思 勳

Fabrication of exfoliated graphene nanomaterials
from graphite and their applications

2013

閔思勳

↑ 2cm ↓

↑ 2.5cm ↓

↑ 4cm ↓

↑ 3cm ↓

↑ 2cm ↓

Fabrication of exfoliated graphene nanomaterials from graphite and their application

by

Sa Hoon Min

Submitted to the Graduate School of Seoul National University in Partial Fulfillment of the Requirements for the Degree of Doctor of Philosophy

January, 2013

Thesis Adviser: Jyongsik Jang

Abstract

Fabrication of exfoliated graphene nanomaterials from graphite and their application

Sa Hoon Min
School of Chemical and Biological Engineering
The Graduate School
Seoul National University

Graphene nanomaterials are fabricated by chemical exfoliation from graphite. In particular, one-dimensional fibrous graphene oxide is obtained by ice-templating of graphene oxide solution, and is reduced by vapor phase reduction without any morphological changes. When the atmospheric Ar plasma is introduced to the one-dimensional graphene oxide, it is also possible to reduce the one-dimensional graphene oxide in less than 10 seconds without toxic reducing agents.

The graphene model for dissipative particle dynamics is proposed by adding additional forces between graphene beads, and is calibrated by structural characteristics analysis. The self-assembly phenomenon between

graphene model and surfactants in aqueous solution is analyzed by dissipative particle dynamics. The self-assembly phenomena of a graphene nanosheet in SDS surfactant solution is predicted, and diverse self-assemblies of graphene/surfactants are also predicted with concentration of surfactants.

Graphene/copper(II) oxide nanocomposite is synthesized using exfoliated graphene oxide by aqueous-phase chemical method. The synthesized CuO had an urchin-like shape densely composed of nano-needles, and the synthesized nanocomposites presented excellent antibacterial performance against both Gram-positive and Gram-negative bacteria. In addition, graphene oxide solution is reduced without reducing agents by mechanical mixing with high speed. It is possible to reduce in diverse solvents, and the product shows high dispersion stability. Reduced graphene oxide solution based ethylene glycol is applied to nanofluids, and the thermal conductivity of the nanofluid with 1 wt% has increased 16.4% compared to that of base fluid.

Keywords: Graphene; Plasma reduction; Dissipative particle dynamics; Antimicrobial; Nanofluid

Student Number: 2007-21187

List of Abbreviations

AAO: anodic aluminum oxide

ATR: attenuated total reflection

CG: coarse-grained graphene

CGNS: coarse-grained graphene nanosheet

CSDS: coarse-grained sodium dodecyl sulfate

CVD: chemical vapor deposition

DMF: N, N-dimethylformamide

DPD: dissipative particle dynamics

EG: ethylene glycol

FE-SEM: field-emission scanning electron microscope

FT-IR: Fourier transform infrared

GO: graphene oxide

H: head

IR: infrared

LN2: liquid nitrogen

NMR: nuclear magnetic resonance

orGO: one-dimensional reduced graphene oxide

oGO: one-dimensional graphene oxide

oprGO: one-dimensional plasma-assisted reduced graphene oxide

prGO: plasma-assisted reduced graphene oxide

RF: radio frequency

rGO: reduced graphene oxide

SDS: sodium dodecyl sulfate

T: tail

TC: thermal conductivity

TEM: transmission electron microscopy

UV-Vis: ultraviolet-visible

XPS: X-ray photoelectron spectroscopy

XRD: x-ray diffraction

List of Figures

and b) formation of the CG bead by grouping six neighboring carbon atoms with c) bond stretch and angle bend limitations. Each bead is linked to six adjacent beads in the CGNS by harmonic springs. Harmonic bend potentials for 60° and 180° angle are applied on the equilateral triangle geometry and the linear form from three neighboring beads, respectively. d) CG beads are shown with spheres by 3D representation.

Figure 23. Bond length between neighboring two CG beads in the CGNS with the spring constant k.

Figure 24. RDF value of the intra-CG beads according to the spring constant $k = 11k_{B}T/r_{c}^{2}$.

Figure 25. Equilibrium morphologies of the CGNSs with angle bend constants.

Figure 26. The contour plot of g(r) for the equilibrium morphologies with the angle bend constants.

Figure 27. a) A spherical CSDS micelle at equilibrium phase with the density field of bead H and b) number density of beads from the center of a CSDS micelle.

Figure 28. Dynamics of the CGNS and CSDS beads in aqueous solution from a random phase. The head groups of the CSDS and tail groups consisting of hydrocarbons are shown with red spheres and sky blue rods,

Figure 37. (a) Low- and (b) high-magnified FE-SEM images of copper(II) oxide prepared under the same condition as in Figure 3 except for the addition of GO solution.

Figure 38. Typical photograph indicating the synthesis of CuO/rGO nanocomposite. The emeraldine $Cu(OAc)_2$ solution turned to deep-blue with adding of ammonia solution and it changed to gray color with hydrothermal reaction at 95 °C for 12 h.

Figure 39. (a,b) TEM and (c-f) FE-SEM images of CuO/rGO nanocomposites prepared under the same condition as in Figure 3 except for different reaction times: (a) pristine GO, (b) 4, (c,d) 8, and (e,f) 18 hour.

Figure 40. Absorption spectra of the methylene blue at different times since the photocatalytic reaction started under irradiation of UV light with assistance of the CuO/rGO nanocomposite.

Figure 41. Photograph images of the zone of inhibition of prepared samples and control by the modified KB test against (a) *E. coli* and (b) *S. aureus*. The sample dispersed aqueous solutions were respectively dropped onto the filter paper and the filter papers were placed on the lawn of bacteria. Distilled water was used for the control. After 24 h of incubation at 37 °C, the zone of inhibition was observed. The filter paper sizes are 10 mm in diameter.

Figure 42. FE-SEM images of *E. coli* (top) and *S. aureus* (bottom) without

nanodispersion and rGO with nanodispersion.

List of Tables

Contents

Chapter 1 Introduction

1.1 Background

1.1.1 Graphene

1.1.1.1 General properties of graphene

Graphene is a monolayer of sp^2-hybridized carbon atoms, having a lattice with a two-dimensional honeycomb-like structure as shown in Figure 1.[1] Owing to its excellent mechanical, electrical and thermal properties, as well as unique structural properties, there has been a rapid increase in interest for graphene nanomaterials. [2-12]

The graphene-based nanocomposites have been widely studied by applying the graphene as a nanofiller, owing to the excellent mechanical properties such as Young's modulus and fracture strength [2]. Moreover, due to the charge carriers mobility and transparent properties,[3] the graphene is one of the most attractive materials in electronic materials. In particular, graphene has also received attention as an outstanding materials for heat exchange and has applied for the nanofluids because of its high thermal

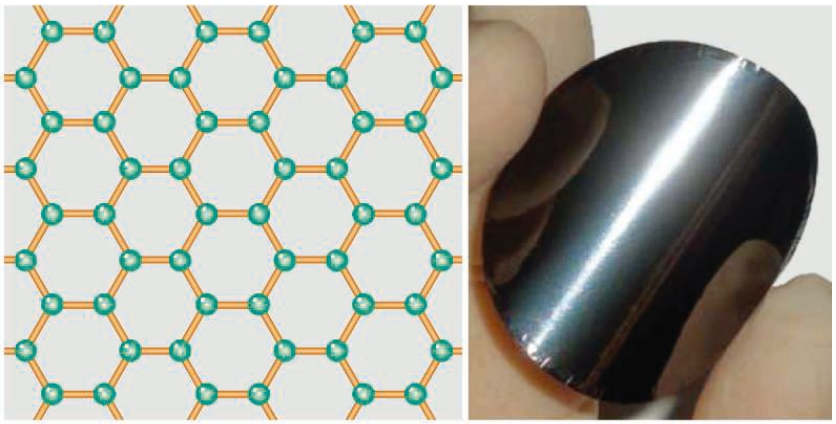

Figure 1. Simple structure of graphene (Left). In graphene, carbon atoms (green dots) are bonded together *via* sp^2 hybridization (orange lines). (Right) Shiny and flexible graphene paper is fabricated by stacking strategy of multi-graphene sheets.[1]

conductivity.[4] In addition, functionalized graphene materials are promising candidates for the application of catalysis,[5,6] energy-storage [7,8] and sensor.[9,10]

1.1.1.2 Synthetic methods for graphene

In general, graphene has been made by three different methods. The first is chemical growth approach (bottom-up preparation) such as chemical vapor deposition (CVD) and epitaxial growth.[13,14] This method make it possible to produce monolayer or few layers of graphene with high quality, but it is not suitable for the mass production. The second method is mechanical exfoliation from graphite (top-down preparation) by Scotch tape.[15] This method can also prepare the graphene with high quality, but it has disadvantage in mass production. The last method is chemical oxidation method (top-down preparation) that makes graphene oxide (GO) from graphite.[23] It is difficult to fabricate high quality graphene because the graphene oxide can not be restored during the reduction process. But this method makes it possible to synthesis the reduced graphene oxide with mass production.

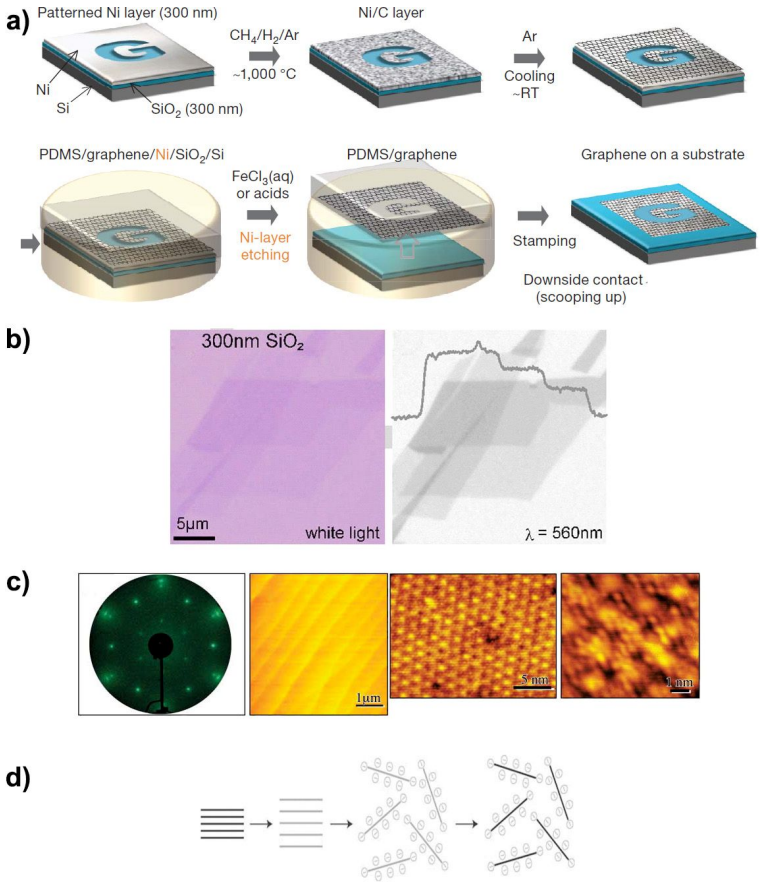

Figure 2. Synthetic method to fabricate graphene nanomaterials by a) CVD,[18] b) micromechanical exfoliation of graphite,[19] c) epitaxial growth on SiC [17] and d) creation of graphene oxide.

1.1.1.3 Graphene oxide

As mentioned above, the graphene oxide has been prepared from graphite oxide, which has been produced by strong oxidation reaction of the graphite. The Brodie,[21] Staudenmaier [22] and Hummers [23] methods are representative approach to fabricate the graphite oxide that can be exfoliated into the monolayer or few layers of graphene oxide by simple ultrasonication.

In the oxidation process, oxygen-containing functional groups such as epoxy, hydroxyl, carboxylic and carbonyl groups would be located the onto the layer of graphite oxide.[50]. Figure 3 shows a well-known structural model for graphene oxide. Among the oxygen-containing functional groups, epoxy and hydroxyl groups are mainly located onto the basal plane of graphene oxide, whereas carboxylic or carbonyl groups are generally attached on the edge of graphene oxide.[11]

1.1.1.4 Reduction of graphene oxide

The GO can be regarded as an intermediate material for the

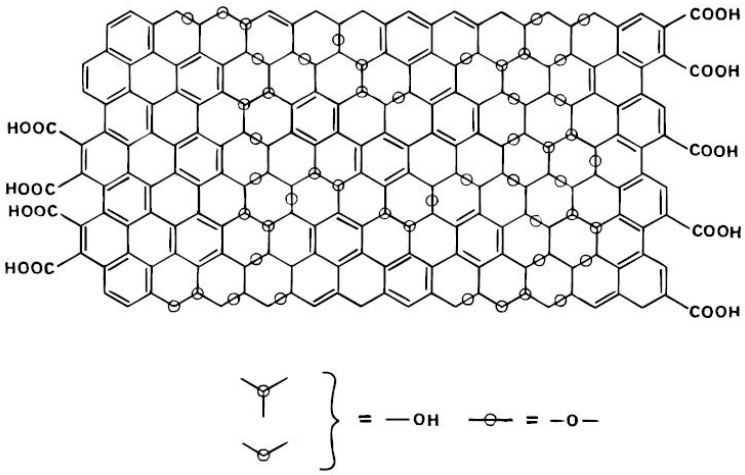

Figure 3. Structural model of graphene oxide possessing the oxygen functional groups.[24]

production of graphene. By removing the oxygen-containing functional groups on the surface, the GO can be restored to the reduced GO (rGO). Various reduction strategies have been investigated to achieve the rGO with high degree of reduction.

The GO has been reduced by two different approaches. The first is thermal treatment such as thermal annealing, heating with microwave and photo-irradiation.[11] Above certain temperature, the GO can be reduced by decomposing the oxygen-containing functional groups with releasing the CO or CO_2 gas. The second is chemical treatment such as chemical reagent,[46] electrochemical [16] and solvothermal reduction.[20] In contrast to thermal reduction, this approach is based on the chemical reaction between strong reducing agents and GO.

However, all of the defects and oxygen-containing functional groups on the GO cannot be restored by thermal and chemical reduction. Therefore, it is still challenging to design a reduction process with high degree of reduction.

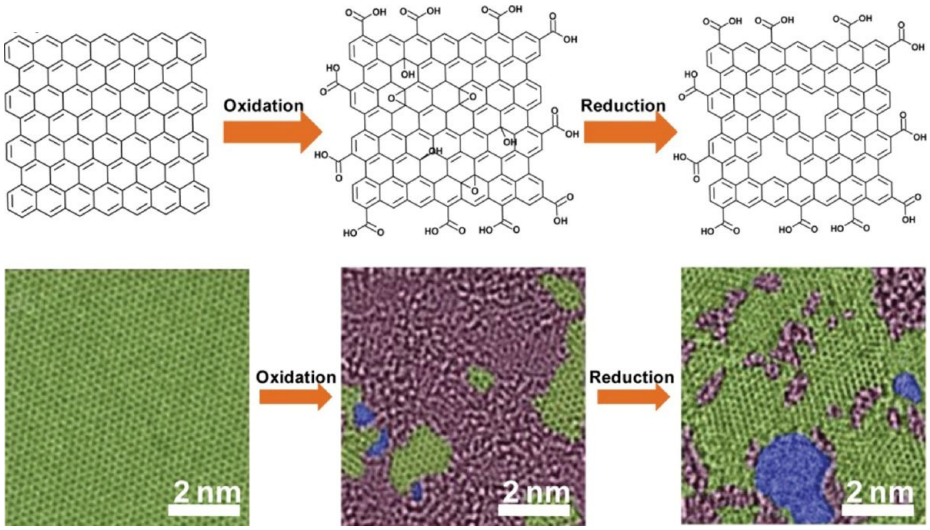

Figure 4. Structural model of graphene (left), GO (middle) and rGO (right). High resolution TEM images with coloring represent the atomic structures of graphene. [33]

1.1.2 Coarse grained molecular dynamics

1.1.2.1 Dissipative particle dynamics

The Dissipative particle dynamics (DPD) methodology was first proposed in 1992 by Hoogerbrugge and Koelman,[26] but the formulation of the equations of motion was incomplete at that time. It was modified and completed by Espanol and Warren,[27,28] and then Warren suggested a numerical algorithm [29] in order to solve the equations of motion for beads. The DPD equation is composed of the sum of dissipative, conservative and random forces. The conservative forces in DPD assigned the soft repulsion between beads. In particular, the combination of dissipative forces and random forces plays a role in maintaining the temperature of simulation box.

The DPD has an advantage to simulate fluids system at a mesoscopic level, because several atoms or repeating units can be represented by a coarse-grained bead. Compared with all-atomic molecular dynamics, the DPD allows simulating a system with large time-scale and length-scale.

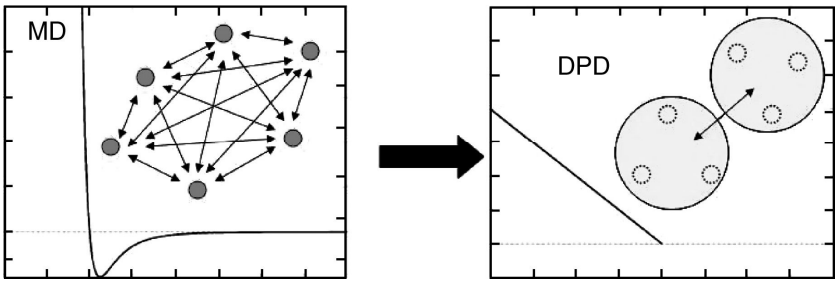

Figure 5. DPD beads representing clusters of atoms or molecules. They interact with each other through soft pairwise forces.[34]

1.1.2.2 Carbon nanomaterials in molecular dynamics

Carbon nanomaterials-based nanocomposites have been attracted a great deal of interest from material scientist over the past decades owing to its excellent physicochemical properties as well as unique structural properties. [1-4] To predict the morphology or calculate the theoretical properties, simulation of carbon nanomaterials have been performed. [35,36]

In term of molecular dynamics, carbon nanomaterials have a relatively large length-scale, except the fullerene. Because of its high computational cost, molecular dynamics with carbon nanomaterials is often limited to the study using all-atomic molecular dynamics. Coarse grained molecular dynamics such as DPD [26] has offered an alternative solution to simulate a carbon nanomaterials-containing system.[36] In particular, DPD would help reduce computational cost effectively, by mesoscale simulation.

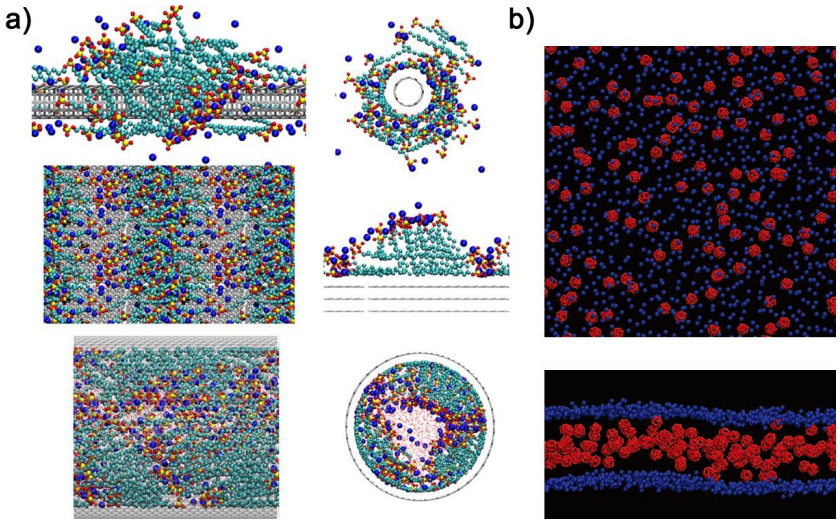

Figure 6. a) Equilibrium morphology of SDS surfactants adsorbed on SWNTs, on graphite and inside SWNTs system, b) Distribution of fullerene in the lipid membrane.[35,36]

1.1.3 Application fields

1.1.3.1 Antimicrobial nanomaterials

Recently, it has attracted considerable interest that decoration of graphene with nano-size metal or metal oxides such as silver,[37,38] palladium,[39] TiO_2,[40] ZnO,[41] and CuO [42] because these graphene-based nanocomposites exhibited remarkable performances as photocatalyst, nanogenerator, electronic sensor and antibacterial agents. In these composite systems, the graphene plays role as a template for synthesis of the metal or metal oxide nanoparticles.[37] The hydroxyl and carboxyl groups located on the graphene oxide can provide binding site for metal precursor; the bound precursors can be nucleation site for the formation of nano-size metal or metal oxide. Ma et al. reported the enhanced antibacterial performance of silver nanoparticles loaded graphene oxide sheets compared with both individual pure silver nanoparticles and graphene oxide.[37] The graphene oxide nanosheet prevents the aggregation of the silver nanoparticles and it easily adheres to bacterial cell by hydrogen bonding, leading enhanced antibacterial efficacy. Moreover, Sun and coworkers present enhanced photocatalytic performance of graphene-TiO_2 nanocomposite.[40] The TiO_2

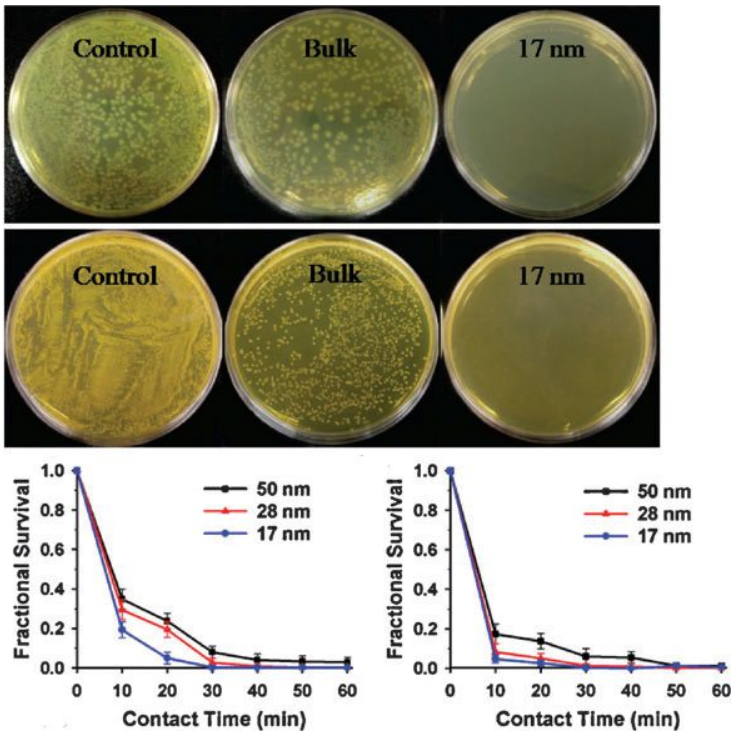

Figure 7. Photographs of the bacterial culture plates of *E. coli* and *S. aureus* (control, bulk powder, and 17 nm silica–polycation core–shell nanoparticles). Antimicrobial kinetic test graphs for the different sized silica–polycation core–shell nanoparticles as a function of contact time against nanoparticle sample.[37]

nanocrystals on graphene oxide sheets can effectively inhibit the charge recombination during photocatalytic process, leading improved photocatalytic efficacy.

1.1.3.2 Nanofluids

Thermal transfer is one of the most important techniques due to its outstanding possibility to handle the heat. In general, the cooling device has established a strategy for maximizing the surface area in order to maximize the heat exchange. In fluid-based cooling device, conventional fluids such as water and EG for heat transfer have relatively low thermal conductivity (TC). Therefore, a large effort has been devoted to enhance the thermal conductivity of the conventional fluids.

Recently, nanofluid that contains nanofillers in conventional fluids has been highlighted for the enhancement of thermal properties. In general, inorganic oxide, metal oxide and metal nanoparticles or CNT have been applied as nanofiller for the nanofluid since the TC of nanofiller is much higher than that of conventional fluids.[43] Because the kind of nanofiller and dispersion stability has a strong influence on the TC of the nanofluid, it

is still challenging to design a novel nanofiller and dispersion strategy.

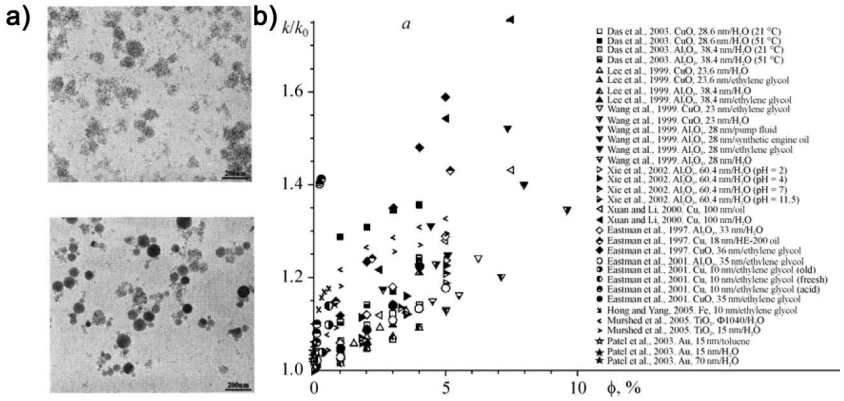

Figure 8. (a) TEM photographs (X50,000) of Al_2O_3 nanoparticles based nanofluid. (b) Enhancement of thermal conductivity for nanoparticle-based nanofluids.[44,45]

1.2 Objectives and Outline of the study

1.2.1 Objectives

The aim of this dissertation proposes novel method to fabricate graphene nanomaterials from exfoliated graphene oxide and to establish graphene model for DPD simulation. One-dimensional graphene nanomaterials are fabricated by ice-templating and are reduced by facile plasma reduction method. In particular, proposed graphene model for DPD simulation are applied to prediction of self-assembly phenomenon between graphene and surfactants in solution. Furthermore, graphene nanomaterials are applied to a substrate for antimicrobial agent and a nanofiller for nanofluid.

1.2.2 Outline

This dissertation focuses on the fabrication of graphene nanomaterials and the establishment of graphene model for DPD simulation and their application. In the viewpoint of abovementioned topics, this dissertation involves the following subtopics;

1. Facile synthesis of one-dimensional graphene network

2. Coarse grained molecular dynamics for graphene/surfactant nanostructure

3. CuO/graphene nanocomposite as an antimicrobial nanomaterials

4. Graphene-based nanofluid for enhancement of thermal conductivity

A detailed outline of the study is as follows:

1. The graphene oxide has been reduced by chemical reducing agent such as hydrazine,[46] sodium boron hydride ($NaBH_4$),[47] lithium aluminium hydride ($LiAlH_4$) [48] or ascorbic acid.[49] In general, chemical reducing agent are toxic to human bodies and environment. Among them, hydrazine has been widely used for reduction process, but it introduces nitrogen-containing functional groups in the graphene structure during the reduction. Therefore several researches focused on the plasma reduction because it did not need toxic chemical reagent and did not remain the nitrogen containing groups. The reduced graphene oxide papers or films have been manufactured.[51-53] However, these reduction processes needed long exposure time (up to 30 min) *in vacuo*, and additional supporting materials

like gold substrate to uphold GO film.[52]

In this dissertation, we report a facile strategy to fabricate one-dimensional graphene nanosheets using freeze-drying process and atmospheric pressure plasma treatment. The morphology of lyophilized GO can be controlled by adjusting the initial concentration of the GO solution. The lyophilized GO with porous structure is reduced by pure argon plasma with no additional chemical reagents and supporter. In order to understand the process conditions of plasma reduction, the degree of reduction was calculated by XPS and Raman analysis.

2. The adsorption of amphiphilic molecules in an aqueous phase is difficult to visualize because it is hard to analyze the adsorbed structures experimentally. Thus, the self-assembly phenomenon and adsorbed morphologies for various amphiphilic molecules have been investigated and predicted using molecular dynamics (MD) simulations.[54,55] Dissipative particle dynamics (DPD) is a type of coarse-grained MD method used to predict a complex fluid system of relatively large length scale and long time scale by replacing several atoms or repeating units with a bead. Recently, several studies have investigated the self-assembly phenomenon between amphiphilic molecules and carbon nanomaterials such as carbon nanotubes

(CNT) [56,57] and fullerene.[58] In particular, hemispherical or cylindrical micellar structure of CNT/surfactant have been predicted by DPD [59] as well as all-atom MD simulations.[60,61] In contrast, relatively little attention has been paid to the graphene nanosheets in the simulation.[62,63]

In this dissertation, we report a DPD simulation for the prediction of the self-assembly between a two-dimensional graphene nanosheet and amphiphilic surfactant molecules in aqueous phase. A coarse-grained graphene model for DPD was proposed by simplifying six carbon atoms with additional forces and calibrated by structural characteristics analysis. The interactions between a graphene nanosheet and a SDS surfactant micelle as well as with surfactant molecules were predicted in order to understand the adsorption process onto graphene nanosheet. In particular, the adsorbed structure of graphene/SDS surfactants was also observed by DPD simulation.

3. Copper oxide a p-type semiconducting material has attracted particular attention because of its useful properties like narrow band-gap and high temperature superconductivity.[64,65] Recently, synthetic methods of CuO/graphene nanocomposite have been actively studied and its unique properties have been applied in various fields such as gas sensor,[66] catalysis,[67] and batteries.[68] In spite of painstaking efforts, only limited

methods have been developed and these methods have drawbacks such as the complicated multi-step procedures, high cost and harsh condition to prepare the nanocomposites. Therefore, developing simple and economical methods for preparation of CuO/graphene nanocomposites is highly desired.

In this dissertation, we report the one-step hydrothermal synthesis of CuO-decorated reduced graphene oxide (CuO/rGO) nanosheet under atmospheric pressure. The evolution process of urchin-like CuO nanostructure was investigated by time-dependent observation using scanning electron microscopy. Notably, copper oxide are the famous antimicrobial agents with other inorganic materials such as silver or ZnO. Ren et al. reported that the nano-CuO effectively kill bacteria *via* releasing of toxic copper ion.[69] We evaluated the antimicrobial performance of the prepared urchin like CuO-decorated rGO nanocomposite against Gram-negative *Escherichia coli* (*E. coli*) and Gram-positive *Staphylococcus aureus* (*S. aureus*). The modified Kirby-Bauer (KB) test and kinetic test were proceeded to investigate the antibacterial activities of as-prepared nanocomposite. Additionally, the morphological changes in the bacteria were investigated after the biocidal test.

4. Wet mixing technology with a high-speed nanodispersion mixer has

received considerable attention in the past decade. High revolution speed of the mixing blade in a chamber provides the formation of a thin film between the wall of chamber and the blade by the shear stress. With the support of this nanodispersion mixer, nanomaterials in suspension can be mixed with a significant energy by the centrifugal force which is greater than gravity.[70]

However, relatively little attention has been paid to the reduction phenomenon induced by the mechanical mixing. This methodology can also make it possible to restrain the aggregation of graphene solution through van der Walls interaction. Simultaneously, the blade raises the temperature of chamber by the high revolution speed, and transfers the energy which can remove the oxygen-containing functional groups and recover the sp^2 structure of the graphene oxide.

In this dissertation, we present a novel methodology for the reduction of GO in the solution phase without any assistant of reducing agents and stabilizers. To the best of our knowledge, this is the first report that GO could be reduced to rGO through a green method *via* a high-speed mechanical mixing process. These graphene solutions were applied as a nanofluid for enhancement of thermal conductivity.

Chapter 2 Experimental Details

2.1 Facile synthesis of one-dimensional graphene network

2.1.1 Fabrication of one-dimensional graphene network

Graphene oxide solution was fabricated by modified Hummer's method.[23] Before the oxidation step, graphite powder (5 g), diphosphoric pentaoxide (2.5 g) and potassium peroxodisulfate (2.5 g) was dissolved in sulfuric acid (30 mL) and the solution was heated to 80 ^{o}C for 6 hr. The pre-oxidized graphite solution was filtered with mixed cellulose acetate filter and remaining graphite powder was kept in vacuum oven for overnight.

The pre-oxidized graphite powder was mixed into sodium nitrate/sulfuric acid solution (21.7 g/L) with vigorous stirring in ice bath. After that, 15 g of potassium permanganate was put into the solution for 10 min, maintaing the temperature lower than 20 ^{o}C. After 30 min, the solution was immediately taken to warm bath (45 ^{o}C) and the color of solution have gradually become grownish gray. After 12 hr, 230 mL of deionized water was carefully put into the solution, maintaining the temperature below 40 ^{o}C,

and additional 700 mL of deionized water was put into the solution. To terminate the oxidation reaction, 25 mL of hydrogen peroxide solution was slowly added to the graphite solution. The solution turned from brown to bright yellow. Then as-obtained graphite oxide solution was washed by using 10 wt% HCl solution three times and deionized water several times with centrifuge until the pH turned to neutral. To exfoliate the layer structure of graphite oxide, the washed solution was sonicated for 1 hr, then the solution was centrifuged with 4000 rpm for 30 min to exclude unexfoliated graphite oxide.

As-obtained homogeneous GO solution (0.5 mg mL^{-1}) was poured into a round flask and was rapidly frozen with liquid nitrogen at -196 ^{o}C. The frozen GO solution was sublimed at -50 ^{o}C under 10 Pa for 2 days with freeze-drying.

2.1.2 Reduction of graphene oxide network *via* argon plasma

For the reduction of GO netwrok by plasma, the lyophilized GO was treated with atomspheric pressure Ar plasma. The plasma treatment condition was fixed as 8 lpm of argon and 200 W of RF power (frequency: 13.56 MHz). The atmospheric plasma was generated by MYPL 200 hand plasma from APP Co.,Ltd. The resultant rGO aerogel was dried in vacuum oven for 1 day to eliminate residual moisture.

In order to make prGO paper, 20 mL of GO solution (0.1 wt%) was filtrated through an AAO membrane filter. After filtration and vacuum drying, paper-like GO was obtained. The prGO was prepared by atmospheric pressure plamsa treatment under the same procedure of rGO aerogel.

JEOL FSM-6701 microscope was used to obtain FE-SEM images. Elemental composition analysis was analyzed by utilizing electron spectroscopy for chemical analysis (SIGMA PROBE, ThermoVG, U.K.). Raman spectroscopy was carried out by using a LabRAM HR spectrometer from Jobin Yvon SA. IR spectroscopy was measured by Perkin-Elmer frontier FT-IR spectrometer and ATR method was applied to investigate the IR spectrum of graphene samples.

Graphite (20 μm of average size) was purchased from Sigma Aldrich

Chemical Co. Hydrochloric acid, diphosphoric pentaoxide, potassium peroxodisulfate, sodium nitrate, sulfuric acid, potassium permanganate, hydrogen peroxide were provided from Samchun chemical Co.

2.2 Coarse grained molecular dynamics for graphene/surfactant Nanostructure

2.2.1 Coarse grained graphene model for dissipative particle dynamics

The force for interacting between the coarse-grained beads for the conventional DPD simulation that was introduced by Hoogerbrugge and Koelman for simple fluid dynamics simulation,[26] is a sum of the three forces in Eq. (1). The conservative force $\mathbf{F}^{C}$ representing a soft repulsion between beads is given by,

$$\mathbf{F}_{ij}^{C} = \alpha_{ij}\omega^{C}(r_{ij})\mathbf{e}_{ij} \qquad \omega^{C}(r_{ij}) = \begin{cases} (1 - r_{ij}/r_{c}) & r_{ij} < r_{c} \\ 0 & r_{ij} \geq r_{c} \end{cases} \tag{1}$$

where α_{ij} is the repulsive interaction parameter between i and j, $\mathrm{r}_{ij} = \mathrm{r}_{i} - \mathrm{r}_{j}$, $r_{ij} = |\mathrm{r}_{ij}|$, unit vector $\mathrm{e}_{ij} = \mathrm{r}_{ij} / r_{ij}$ and r_{c} is cutoff radius. The bead density ρ set as 3. The repulsive interaction parameter α_{ij} and the Flory-Hyggins χ parameter has a linear relationship as follows,[71]

$$\alpha_{ij} = \alpha_{ii} + 3.27\chi_{ij} \tag{2}$$

where α_{ii} is usually established to $25k_BT$ for representing the compressibility of water. The interaction parameters between coarse-grained beads was set from the literature[72] and summarized in Table 1. The dissipative force $\mathbf{F}^D$ representing a hydrodynamic drag is given by,

$$\mathbf{F}_{ij}^{D} = -\gamma_{ij}\omega^{D}(r_{ij})(\mathbf{e}_{ij} \cdot \mathbf{v}_{ij})\mathbf{e}_{ij} \quad \omega^{D}(r_{ij}) = \begin{cases} (1 - r_{ij}/r_c)^2 & r_{ij} < r_c \\ 0 & r_{ij} \geq r_c \end{cases} \tag{3}$$

where γ is strength of the dissipative force set as 4.5, relative velocity $v_{ij} = v_i - v_j$. The random force $\mathbf{F}^R$ representing a thermal noise is given by,

$$\mathbf{F}_{ij}^{R} = \sigma_{ij}\omega^{R}(r_{ij})\xi_{ij}\frac{1}{\sqrt{\Delta t}}\mathbf{e}_{ij} \quad \omega^{R}(r_{ij}) = \begin{cases} (1 - r_{ij}/r_c) & r_{ij} < r_c \\ 0 & r_{ij} \geq r_c \end{cases} \tag{4}$$

$$\begin{gathered} \sigma^2 = 2\gamma k_B T \\ \langle \xi_{ij}(t) \rangle = 0, \ \langle \xi_{ij}(t)\xi_{ij}(t') \rangle = (\delta_{ik}\delta_{jl} + \delta_{il}\delta_{jk})\delta(t - t') \end{gathered} \tag{5}$$

where ξ_{ij} is randomly fluctuating variable with Gaussian statistics, value of 3 is used for the random noise strength σ. The combination of dissipative

forces and random forces in DPD simulation consitutes a thermostat, which holds the temperature of simulation box.[27]

Table 1. Interaction parameters α_{ij} of Eq. 1 between the coarse-grained beads.

	CG	**H**	**T**	**Water**
CG	25	40	25	80
H	40	27	40	25
T	25	40	25	80
Water	80	25	80	25

2.2.2 Self-assembly phenomenon between graphene and surfactant by dissipative particle dynamics simulation

A modified version of velocity-Verlet algorithm was applied to this study, in order to integrate the equations of motion for the beads.[73] The masses of the beads m_i, the thermal energy $k_B T$ and the cutoff radius r_c was taken as units of mass, energy and length, respectively, thus natural unit of time could be calculated as follows,

$$\tau = r_c \sqrt{m_i / k_B T} \tag{6}$$

but they were converted to the physical units for better understanding.

In this study, five water molecules were set as a single coarse-grained W bead. Any partial charge or charge were not assigned to all of the coarse-grained beads. The CSDS was composed of one H bead and three T beads, representing the amphiphilic surfactant molecule. The Na^+ ions as counterions of SDS molecules were omitted from this simulation, because they has been situated close to the head groups.[63,74]

To represent the weak repulstion force between the head groups, the interaction parameter between H beads was set as 27, according to the

literature.[59] The spring constant k for the bonding of H-T and T-T of the CSDS was set as $10k_BT$. For the rigidity of the SDS molecule, the angle bend constants for H-T-T and T-T-T conformation was set to $5k_BT/\text{rad}^2$. All simulations were calculated in a simulation box ($30r_c \times 30r_c \times 30r_c$) except the calibration step for graphene, and were carried out in periodic boundary conditions using *Materials Studio* software.

2.3 CuO/graphene nanocomposite as an antimicrobial nanomaterial

2.3.1 Fabrication of CuO/graphene nanocomposite

In a typical procedure, GO was synthesized from graphite using a modified Hummers method.[75] To synthesis the CuO/rGO composite, 0.66 mmol of copper(II) acetate ($Cu(OAc)_2$) was dissolved in deionized water (40 mL) at room temperature. Then, the GO solution (22 mg/mL) was injected to the green $Cu(OAc)_2$ solution and stirred for 30 min. The 10 mL of ammonia solution (14 ~ 15 %) was slowly dropwised into the aqueous solution. After 1 h of stirring, the mixed solution was immersed in a pre-heated oil bath (95 ^{o}C) and remained in the bath for 12 h with magnetic stirring. After the reaction, the synthesized CuO/graphene nanocomposite was centrifuged and washed with an excess amount of water to remove residual reagents and neutralize the solution. In our experimental condition, the rGO was prepared as same condition as mentioned above without addition of $Cu(OAc)_2$.

Energy-filtering transmission electron microscopy (EF-TEM) images were obtained with a Carl Zeiss LIBRA 120 at an acceleration voltage of 120 kV. In the sample preparation, CuO/graphene nanocomposite was cast onto a

copper grid after dilution in aqueous solution. Field-emission scanning electron microscopy (FE-SEM) images were obtained using a JEOL 6700 at an acceleration voltage of 10 kV. The X-ray diffraction (XRD) was obtained with a D8-Advanced (Bruker Miller Co., U.K.). Raman spectra were observed with Triax550 (HORIBA, Ltd., Japan).

2.3.2 Antimicrobial properties of CuO/graphene nanocomposite

The microorganisms were cultivated in sterilized in Luria–Bertani (LB) broth and then incubated overnight at 37 °C with a shaking incubator. The 1 mL of bacterial suspensions employed for the antibacterial experiments contained from 10^6 to 10^7 colony forming units (CFU). For the bacterial test, the prepared nanocomposite (1 mg) were dispersed in 1 mL of sterilized water and inoculated with 100 μL of bacterial suspension (*E. coli*, and *S. aureus*) which has concentration to 10^6 to 10^7 CFU/mL. The rGO dispersed solution (1 mg/mL) was prepared and tested as a comparative material. A blank solution was also prepared as an experimental control. The bacteria-inoculated solutions were incubated in a shaking incubator at 37 °C. After a specific contact time, 50 μL aliquots were taken from each tube and cultured on LB agar plates. The LB agar plates were kept overnight at 37 °C and the number of grown bacterial colonies was observed and counted.

Additionally, each solution after 1h of antibacterial test was drop-cast on the surface of the silicon wafer and dried. Then, the bacteria were then fixed in 2.5% glutaraldehyde for 2 h and rinsed several times with distilled water. Post-fixation proceeded for 1 h with 1% osmium tetroxide in distilled water. After fixation, the samples were dehydrated with ethanol (20–100%),

air-dried, and sputter-coated with platinum/palladium for FE-SEM observation.

For the modified KB test, the filter papers were respectively dip-coated with the suspensions of the CuO/rGO nanocomposite, rGO and GO (3 mg/mL). The paper dipped in distilled water was prepared as control. Then, the dried filter papers were gently placed on the *E. coli* and *S. aureus* growth LB agar plate. After 24 h of incubation, the zone of inhibition was observed.

2.4 Graphene-based nanofluid for enhancement of thermal conductivity

2.4.1 Fabrication of mechanical reduced graphene oxide using nanodispersion technique

Graphite oxide was fabricated from natural graphite by a modified Hummers method.[23] The graphite oxide solution was centrifuged at 4800 rpm for 30 min, and the remains was washed with 1 M HCl for 3 times and warm water for 5 times until the pH value of the suspension closed to 7. The obtained graphite oxide paste was dispersed in deionized water and exfoliated by ultrasonication for 1 h. a homogenous GO suspension was obtained after filtration the black residual powder, indicating unoxidized graphite.

As-synthesized GO powder was re-dispersed in deionized water or EG with magnetic stirring for 12 h, then mild sonication was applied to the solution for 30 min to ensure well dispersion.

The mechanical reduction was carried out by the wet mixing technology using a nano dispersion mixer (T.K.FILMICS 56, PRIMIX) without any reducing agent. The 70 mL of GO solution (5 g/L) was put into

the reactor of the mixer, and then the solution was mixed with 18400 rpm. The mixing time was adjusted from 10 min to 60 min in order to confirm the degree of reduction. The temperature of the solution rapidly increased about 100 ^{o}C for water and 143 ^{o}C for EG, when the mixing started. The reduced GO samples were collected with centrifuge and freeze-drying method.

X-ray diffraction was analyzed with Rigaku X-ray diffractometer with CuKα target. Raman spectra were measured by Jasco NRS-3200 Raman spectroscopy using a 633 nm helium-neon laser. Solid-state ^{13}C NMR experiments were performed with a JEOL ECA400 spectrometer operated at 100.53 MHz using the single pulse decoupling method. The elemental composition was obtained from the CHN elemental analysis (Yanako MT2 CHN Corder, Japan). X-ray photoelectron spectroscopy (XPS) spectra were measured by a JEOL JPS-9000MC instrument equipped with an MgKα X-ray source. The structure of GO and rGO was observed under a field-emission scanning electron microscope (SEM; JEOL-6300F, 3 kV) and a high resolution transmission electron microscope (TEM; JEM-2010F, 200 kV).

2.4.2 Enhancement of thermal conductivity for the graphene-based nanofluid

The thermal conductivity of graphene-based nanofluids, containing GO and rGO were measured by the transient hot wire method. The Pt wire in the measurement device was coated with a thin Teflon layer for insulation. The change of resistance of the Pt wire was calculated by measuring the voltage drop from a Wheatstone bridge using nanovoltmeter (2182A, Keithley Co.). A temperature profile was calculated by the Bentley equation.[106] The TC can be defined as follows,

$$\lambda = (q / 4\pi) / (d\Delta T / d(\ln t)) \tag{7}$$

Where λ is TC, q is the heat generated per unit length of Pt wire, $d\Delta T$ is the temperature difference of Pt wire, and t is time.

Chapter 3 Results and Discussion

3.1 Facile synthesis of one-dimensional graphene network

3.1.1 Fabrication of one-dimensional graphene network

The overall synthetic process to fabricate one-dimensional reduced GO (orGO) is represented in Figure 9. Aqueous dilute graphene oxide solutions were frozen in LN2 condition. One-dimensional graphene oxide (oGO) with fibril morphology was obtained by low concentration of GO solution after freeze drying process. Then the oGO was reduced by vapor phase reductions using two-step method.

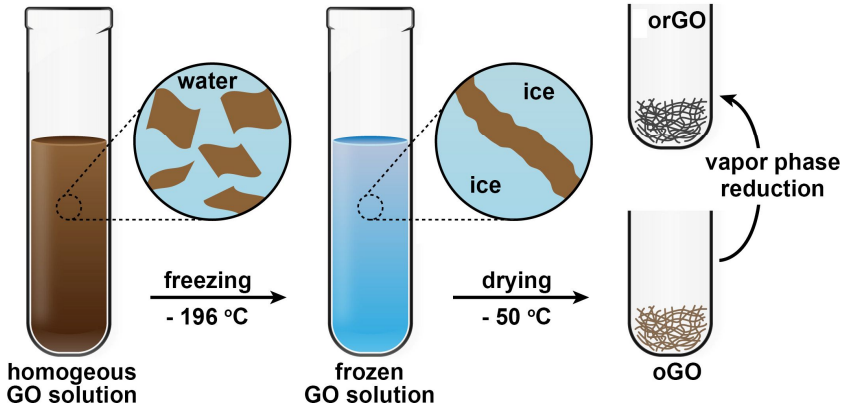

Figure 9. Schematic illustration of synthetic procedure for fabricating the oGO network by freeze drying process and vapor phase reduction.

Figure 10a shows the SEM image of oGO sample (0.5 mg/mL) with micro-fibril structure. The width of the oGO was about 1 μm. This morphology is similar to polymeric micron fibers from ice-templating. In the fast solidification of polymeric solution by supercooling, it is recognized that the interface between solvent and nanofiller becomes unstable, making aligned dendritic nano-structure.[76] Therefore, polymer microfibers could be fabricated after freeze-drying process. However, in the case of fast solidification for graphene oxide solution, two-dimensional aligned structure would be formed owing to the structure of graphene oxide. The lyophilized oGO could be easily redispersed in polar solvents because of its porous structure. So, the reduction was conducted in vapor phase of hydrazine (not in solution phase) in order to maintain the one-dimensional structure. After vapor phase reduction process, the one-dimensional reduced graphene oxide (orGO) was obtained. There was no difference in the morphology between the oGO and orGO as shown in Figure 10b.

The SEM image without Pt-Pd sputtering and the TEM image of the orGO indicated that the orGO was composed of few-layer of graphene sheets (Figure 10c and 10d). Because the GO sheets in suspension was aligned and rejected from the ice-template during the fast solidification, GO sheets might be stacked mutually in the template. Therefore, orGO as a reduced form of

oGO also had thin and on-dimensional morphology.

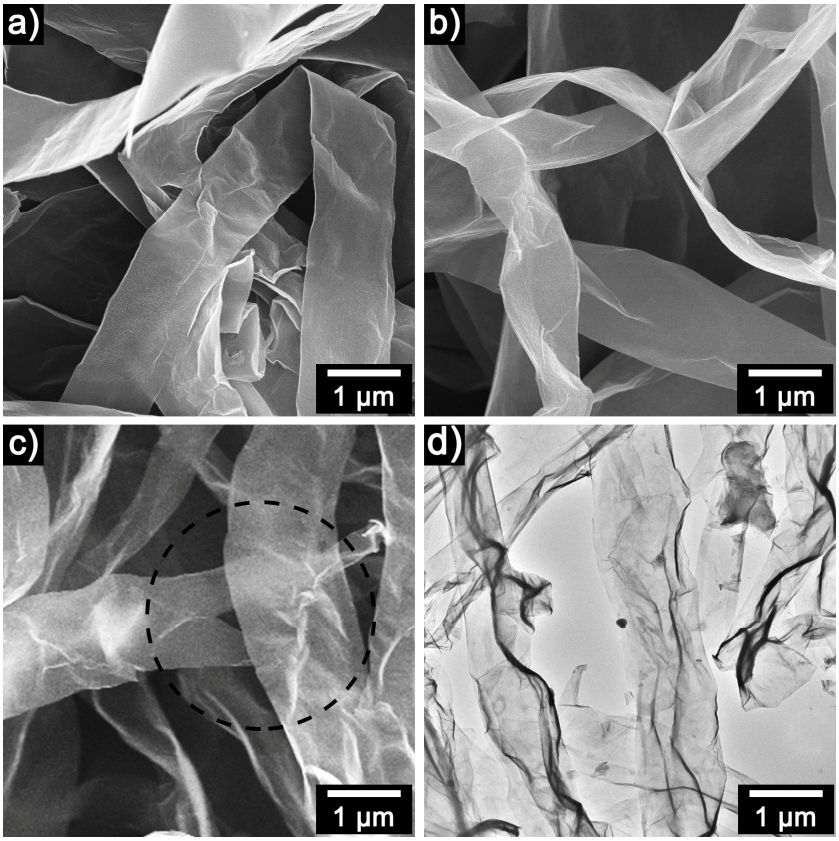

Figure 10. SEM image of a) oGO, b) orGO and orGO without Pt-Pd sputtering. d) TEM image of orGO.

To clarify the formation mechanism of one-dimensional morphology, the GO solution was lyophilized with different initial concentration. At high concentration (10 mg/mL), the morphology of lyophilized GO was mainly planar type as shown in Figure 11a. The planar lyophilized GO was turned into one-dimensional shape and the width of that decreased with decreasing the initial concentration of GO solution. In general, as the concentration of a polymer solution decreased, the diameter of polymeric fiber also decreased since the small number of polymer molecules was assembled and stacked in the fast solidification.[77] However, in the case of the GO solution, the lyophilized products showed a morphological transition from planar shape to one-dimensional structure as the initial concentration decreased.

Figure 12 shows the XRD pattern of lyophilized GO with different concentration. At high concentration, The XRD pattern of the lyophilized GO (10 mg/mL) showed a strong peak at $2\theta = 13.5^{o}$, indicating the interlayer structure of GO sheets. As the initial concentration decreased, the typical GO peak in the XRD pattern had become weaker, meaning that the population of stacked GO structure decreased. These results suggest that two-dimensional GO sheets are stacked in the ice-template during the fast solidification. At the high concentration, a large number of individual GO sheets are assembled and form a planar structure. As the concentration decreases, the

individual GO sheets would be aligned with an aligned with a direction in ice-template rather than be stacked.

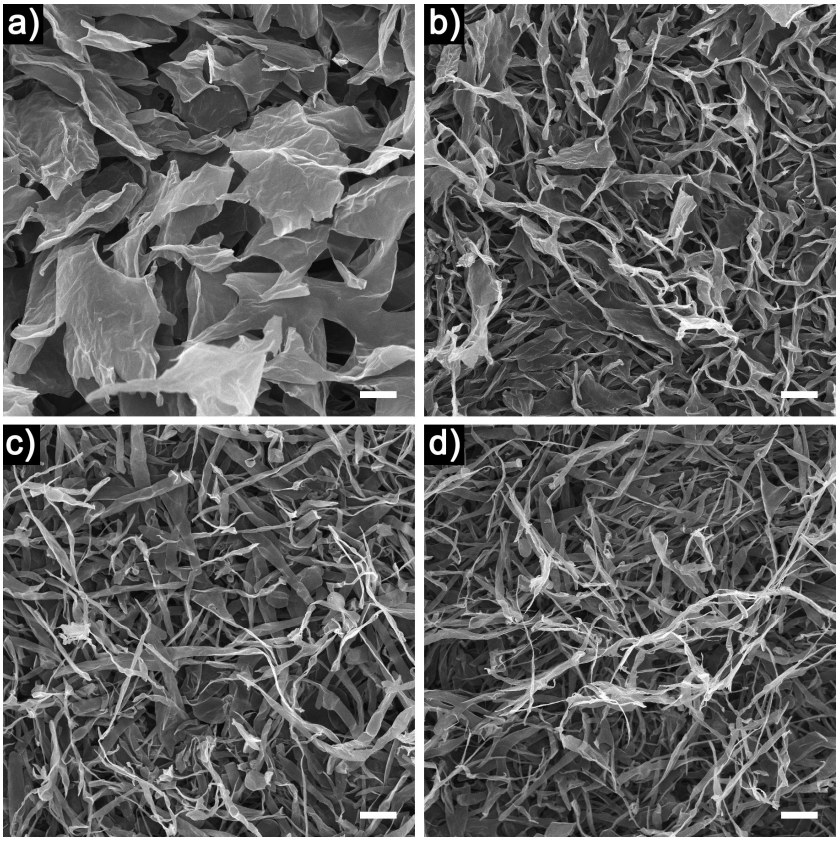

Figure 11. SEM images of the lyophilized GO with different concentrations: a) 10 mg mL^{-1}, b) 5 mg mL^{-1}, c) 2.5 mg mL^{-1}, and d) 0.5 mg mL^{-1} (scale bar: 5 μm).

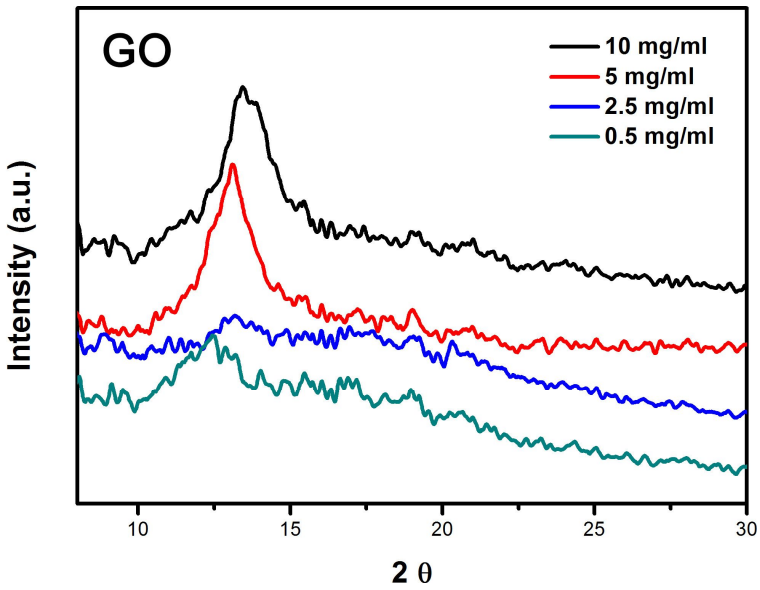

Figure 12. XRD patterns of lyophilized GO with different concentrations.

3.1.2 Reduction of graphene oxide network *via* argon plasma

Figure 13 represents the process of plasma-assisted reduction of oGO. GO solution was prepared by modified Hummer's method, as already described in section 2. The dark brown GO solution was diluted to 0.05 wt% for formation of one-dimensional structure after freeze-drying step. As shown in Figure 14a, the brownish-grey oGO could be obtained after the freeze-drying.

The one-dimensional plasma-assisted reduced graphene oxide (oprGO) was fabricated by atmospheric-pressure argon plasma with gas flow rate of 8 L/min. When the argon plasma curtain reached the oGO, the color of oGO was rapidly turned from brownish-grey to black, as shown in Figure 14b. In the process of the formation of argon plasma, the argon gas would turn into argon ions with electrons. Therefore, it is expected that the vast amount of electrons can eliminate the oxygen functional groups on the surface of oGO. Because of the low energy potentials and kinetic energies of plasma, it has been reported that the plasma treatment is sufficient for processing atomically thin nanomaterials such as GO.[78]

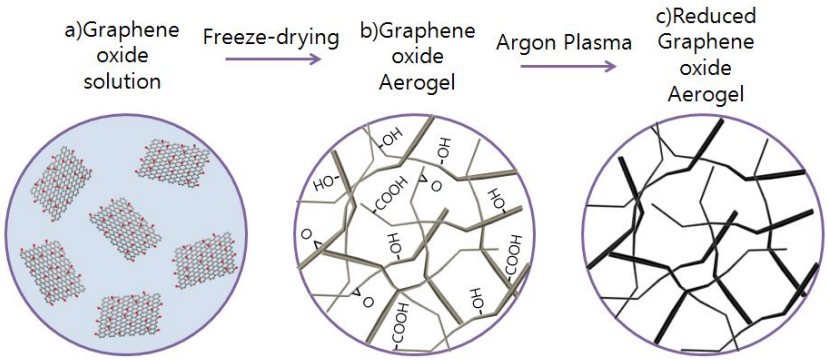

Figure 13. A schematic illustration of plasma-assisted reduction of oGO. a) The homogeneous GO solution. b) The collected oGO after freeze-drying for 48 hrs. c) The oprGO aerogel after in contact with plasma curtain for 3 seconds. The reduction of oGO was recognized by color change of GO materials.

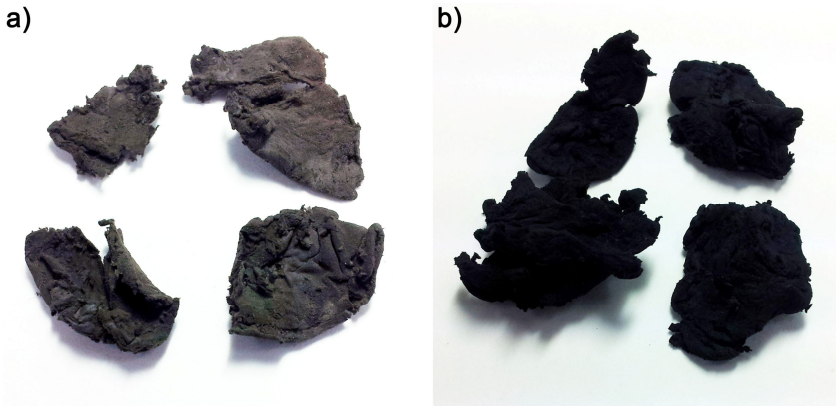

Figure 14. Photographs of a) oGO and b) oprGO.

To observe the nano-structure of oGO before and after the plasma treatment, SEM images were taken. In Figure 15a, the oGO represents a micro-fibril structure with about 1 μm of width, as mentioned above. This morphology clearly indicates that the oGO is fabricated with ice-templating.

However, the oprGO was expanded to about three times its original size by the treatment of atmospheric-pressure argon plasma, as shown in Figure 15b. It is believed that the rapid reduction by plasma treatment makes the sudden elimination of oxygen functional groups on the GO, thus the gases from the oxygen functional groups extended the stacked layers of the GO. Nevertheless, the percolated network was well preserved and no visible morphological transition was observed.

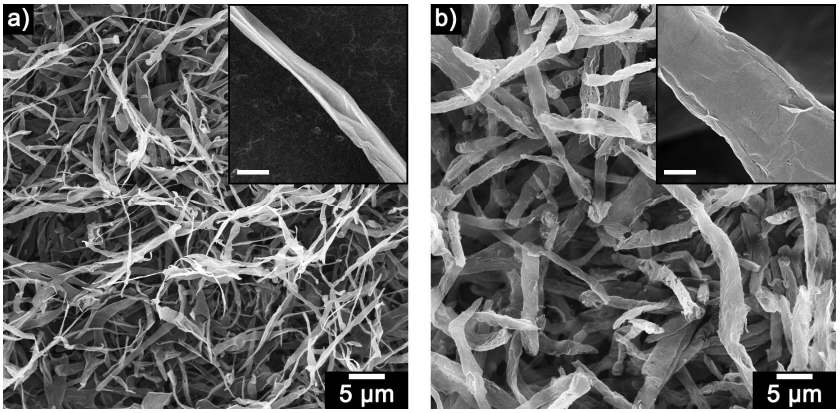

Figure 15. SEM images of a) oGO and b) oprGO network. The both inset images show highly magnified (×20,000) structures. (scale bar: 500 nm) The difference between width of GO sheets in a) and b) was due to the plasma treatment.

The minimum power and exposure time required to conduct the reduction of oGO was investigated by XPS analyses. First, the C1s analysis of oprGO with applied plasma power was demonstrated in Figure 16. In the pristine oGO spectrum, 284.5 eV and 286.5 eV was highlighted, indicating the C-C/C=C bonding and C-O bonding, respectively, as reported in previous works.[52,79] This tendency was kept until the power increased from 80 W to 120 W.

From 140 W of plasma power, the C-O bonding was attenuated and the C1s peak related to the C-C/C=C bonding increased. Although the weak peak at 287.8 eV and 290 eV, indicating the characteristic of C=O and C(COOH) functional groups were still remained, the overall peak related to the oxygen groups was decreased. Moreover, the color of oGO did not turn into black under 140 W. Applying above 140 W, however, the color of oGO changed to black, which indicated the formation of rGO. And the C/O ratio of oprGO was increased to about 6 in more than 140 W. Judging from these results, it is considered that the minimum required power for the reduction is 140 W.

Figure 17 shows the C/O ratio of oprGO with applied plasma power and exposure time, to further explore the effect of plasma conditions. The C/O ratio was increased to almost two times in the range of 120 ~ 150 W.

However, in the range of 150 ~ 300 W, there is no significant change of C/O ratio with the increase in plasma power, as shown in Figure 17a. It can be inferred that applying more than 150 W is not effective to cleave more oxygen functional groups onto the GO.

The dependence of the degree of reduction with exposure time was also investigated. The C/O was rapidly increased until 5 seconds. Similarly, there is no additional increment with more plasma exposure. From these results, it can be concluded that the plasma-assisted reduction in this condition can reduce the GO in less than 10 seconds with 150 W. To further investigate the tendency on the degree of reduction with applied plasma power, C1s analysis was additionally conducted and calculated C/O ratios from oprGO and prGO paper, summarizing in Table 2.

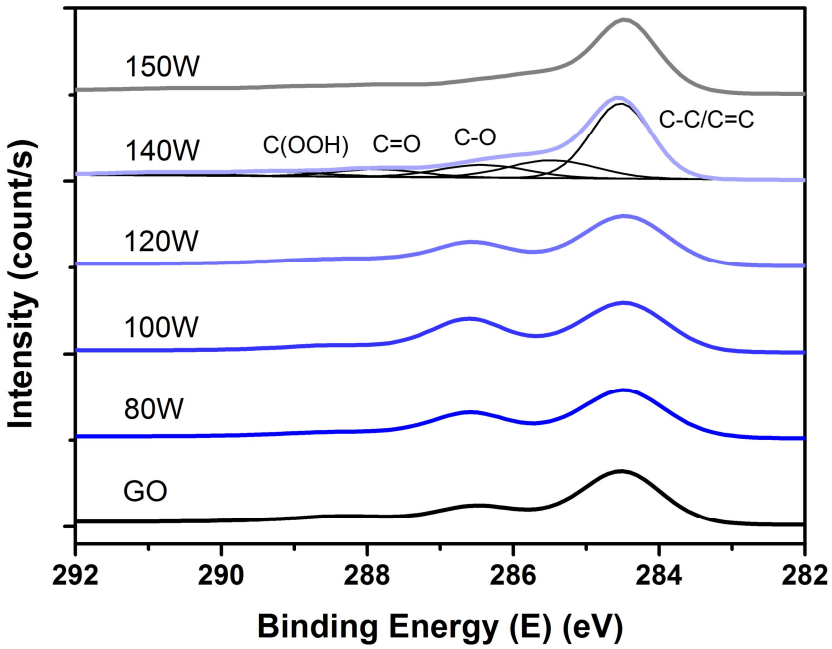

Figure 16. XPS C1s spectra of oprGO with various plasma powers from 80 W to 150 W.

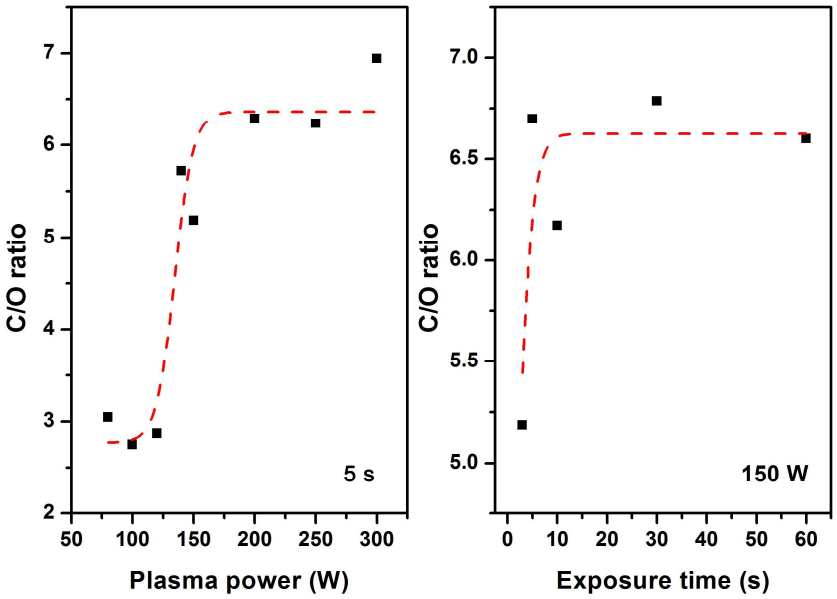

Figure 17. a) C/O ratio of oprGO with applied plasma power and b) with exposure time at 150 W.

Table 2. C/O ration of oprGO and prGO paper with plasma power and exposure time.

Plasma power/exposure time	C	O	N	C/O ratio	C/N ratio
150W / 3s	83.25	16.05	0.7	5.186916	118.9286
150W / 5s	86.47	12.91	0.63	6.697909	137.254
150W / 10s	85.51	13.85	0.64	6.174007	133.6094
150W / 30s	87.15	12.84	0	6.787383	
150W / 60s	86.85	13.16	0	6.599544	
200W / 3s	85.8	13.64	0.57	6.290323	150.5263
200W / 5s	85.51	14.49	0	5.901311	
200W / 10s	88.14	11.86	0	7.431703	
250W / 3s	86.18	13.82	0	6.23589	
250W / 5s	87.51	12.49	0	7.006405	
250W / 10s	88.6	11.41	0	7.765118	
300W / 3s	87.41	12.59	0	6.942812	
300W / 5s	85.31	13.78	0.91	6.190856	93.74725
300W / 10s	83.18	16.02	0.81	5.19226	102.6914
80W / 3s	74.65	24.51	0.84	3.045696	88.86905
100W / 3s	72.83	26.46	0.7	2.752457	104.0429
120W / 3s	73.45	25.58	0.97	2.871384	75.72165
140W / 3s	84.77	14.82	0.41	5.719973	206.7561
GO aerogel	74.47	25.09	0.44	2.968115	169.25
Plasma RGO paper	79.97	19.59	0.44	4.08218	181.75

For comparison with non-porous GO, the prGO paper was additionally fabricated from GO paper and analyzed with Raman spectra. Figure 18 represents the Raman spectra of pristine oGO, oprGO and prGO paper. In Raman analysis, the D peak at 1335 cm^{-1} and the G peak at 1600 cm^{-1} were observed in every sample, indicating the defect and the graphitic region of the GO, respectively. The I_D/I_G values were calculated from the intensity ratio of the D peak to the G peak of Gaussian curve-fitting for the Raman spectra. In the case of oprGO, the intensity of D peak was attenuated with decreasing the ratio from 1.363 to 0.964, indicating that the defective region of GO was restored by plasma treatment.

Compared to I_D/I_G value of the oprGO, the prGO had higher ratio (ca. 1.086), which means the degree of reduction of prGO was lower than that of oprGO. The GO paper could be not fully reduced in less than 10 seconds. As the atmospheric plasma was treated with same condition, it can be inferred that the porous oGO has an advantage in contact with plasma ions.

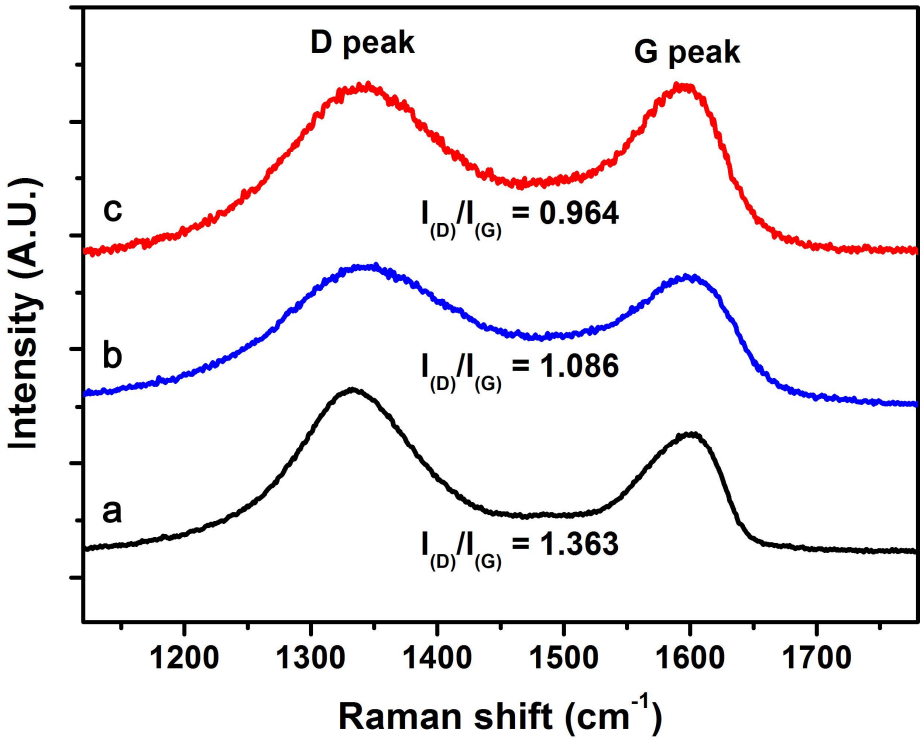

Figure 18. Raman spectra of a) Pristine oGO, b) prGO and c) oprGO with plasma treatment. (200 W, 5 s) I_D/I_G values in the Raman spectra calculated from the curve-fitted intensity ratio of D peak to G peak.

The state of chemical bonding for the plasma treated GO samples was also analyzed by XPS spectra to support the Raman analysis. Figure 19 shows the XPS C1s spectra of pristine oGO, oprGO and prGO paper. In oGO spectrum, the peak at 286.5 eV corresponding to the C-O has 14.1% of peak area. In the case of oprGO, that peak diminished to 7.1%, while the peak at 284.6 eV indicating the C-C/C=C in graphene structure slightly increased from 45.9% to 52.6% after plasma reduction. On the other hand, the XPS peak related to the C-O in prGO has 12.8% of peak area, which is more close to the area of oGO.

This tendency is similar to the result of Raman analysis, representing the lower degree of reduction of prGO paper. Owing to the stacked structure of GO paper,[80] it would be hard to penetrate plasma ions into the GO sheets, whereas the porous structure of oGO allows easy access for plasma ions.

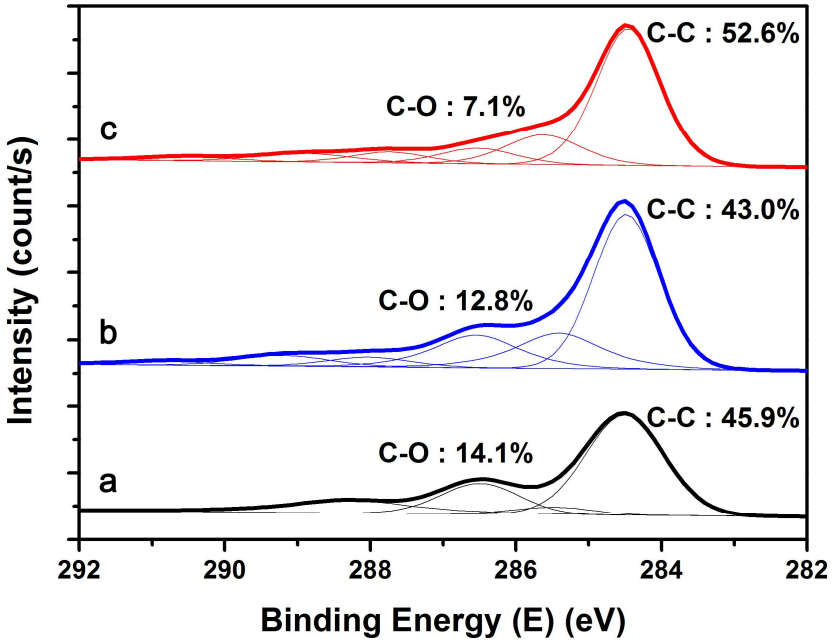

Figure 19. XPS analysis of a) Pristine oGO, b) prGO and c) oprGO. The percentages of bond peak were calculated by integrating the area under peak curve.

The cleavage of oxygen functional groups was also observed by ATR FT-IR measurement. In Figure 20, FT-IR spectra for oGO, oprGO, prGO paper and orGO by hydrazine were exhibited. There is a broad peak at 3400 cm^{-1} corresponding to O-H stretching vibration in oGO and prGO paper. This hydroxyl groups were absent in oprGO, indicating the high degree of reduction.

Additionally, the peak related to nitrogen functional groups were also absent in oprGO in XPS N1s analysis, whereas various nitrogen-containing functional groups were found in orGO by hydrazine, as shown in Figure 21. Because it is known that the hydrazine could add the nitrogen-containing functional groups to the rGO during the reduction reaction, this plasma reduction would be an alternative to produce pure rGO.

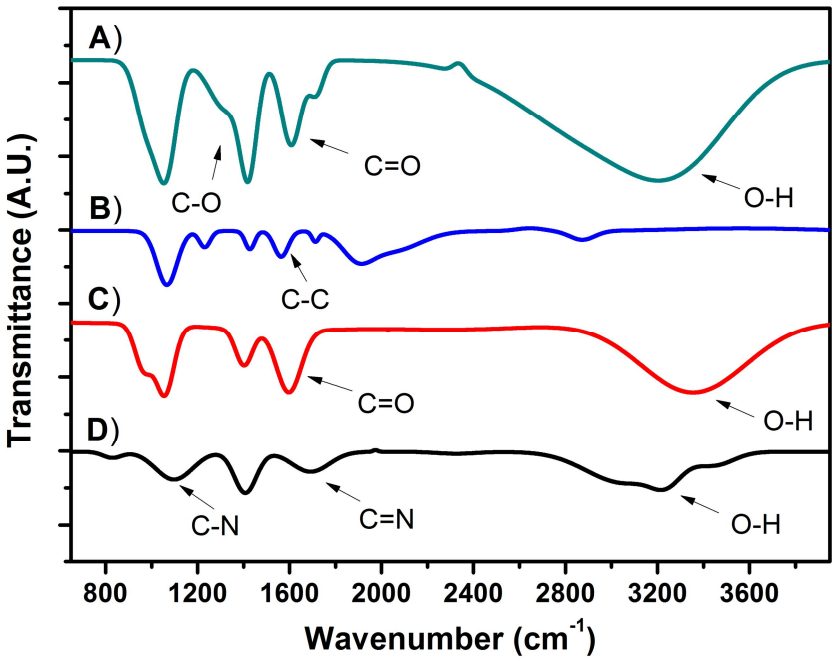

Figure 20. ATR-FTIR analysis of a) oGO, b) oprGO, c) prGO paper and d) orGO by hydrazine.

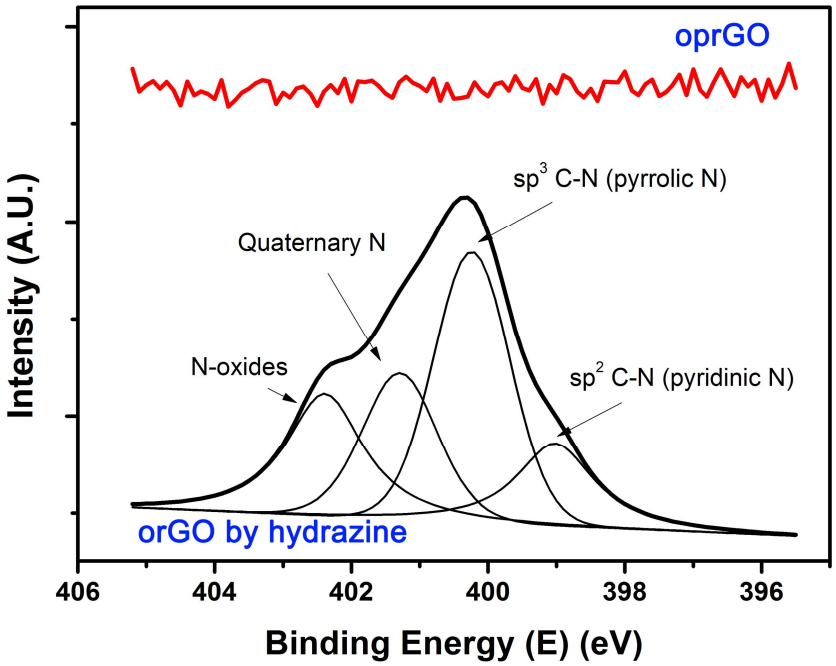

Figure 21. XPS N1s spectra of oprGO and orGO by hydrazine.

3.2 Coarse grained molecular dynamics for graphene/surfactant nanostructure

3.2.1 Coarse grained graphene model for dissipative particle dynamics

In this study, the DPD model for graphene is based on the soft beads proposed by Groot and co-workers.[29] The motion of the beads in the simulation box is expected by solving Newton's equations of motion for each bead,

$$\frac{d\mathbf{r}_i}{dt} = \mathbf{v}_i \qquad m_i \frac{d\mathbf{v}_i}{dt} = \mathbf{f}_i \tag{8}$$

where $\mathbf{r}_i$ is the position of bead i, $\mathbf{v}_i$ is its velocity, m_i is its mass, and $\mathbf{f}_i$ is the total force on bead i. The force can be calculated as the sum of three non-bonding forces (conservative repulsive, dissipative, and random forces) that influences each pair of beads, according to

$$\mathbf{f}_i = \sum_{j \neq i} (\mathbf{F}_{ij}^{\mathrm{C}} + \mathbf{F}_{ij}^{\mathrm{D}} + \mathbf{F}_{ij}^{\mathrm{R}}) + \mathbf{F}_i^{\mathrm{S}} + \mathbf{F}_i^{\mathrm{A}} \tag{9}$$

where $\mathbf{f}_i$ is the total force on bead i, and $\mathbf{F}^C_{ij}$, $\mathbf{F}^D_{ij}$, and $\mathbf{F}^R_{ij}$ are, respectively, the conservative force, the dissipative force, and the random force. In order to represent the interactions between connected beads, the spring force ($\mathbf{F}^S_i$) and angle force ($\mathbf{F}^A_i$) are introduced to DPD simulation.

Figure 22 displays the scheme for the bead formation and inter-connection between beads for DPD modeling of the coarse-grained graphene nanosheet (CGNS). In order to establish the CGNS model, every six neighboring carbons like a benzene ring in the graphene were modeled as a coarse-grained graphene (CG) bead, as shown in Figure 22b. In general, different beads grouping by several atoms should have equal volume for the relationship between Flory-Huggins interaction parameter and repulsion parameter in DPD simulation.[29] Because molecular volume of benzene molecule is about 148 Å^3, reference volume for one bead has been set as 150 Å^3, which equals to that of fiver water molecules. In Figure 22c, each CG bead is connected to six adjacent beads by Hookean spring,

$$\mathbf{F}_i^S = -\partial U^S / \partial \mathbf{r}_i \qquad U^S = \sum \frac{1}{2} k(\mathrm{r} - \mathrm{r}_0)^2 \tag{10}$$

where U^S is the total bonded potential, the equilibrium distance r_0 is set to

zero, and k is the modulus of the spring. In order to hold the honeycomb structure and two-dimensional properties of graphene during the simulation, two types of angle-bend interactions between beads were introduced into the DPD simulation:

$$\mathbf{F}_i^{\mathrm{A}} = -\partial U^{\mathrm{A}} / \partial \mathbf{r}_i \qquad U^{\mathrm{A}} = \sum \frac{1}{2} k_\theta (\theta - \theta_0)^2 \tag{11}$$

where U^{A} is the total angular potential, θ_0 is the equilibrium angle, and k_θ is the angle bend constant. The equilibrium angles for the equilateral triangle and the linear structure from three neighboring CG beads were 60° and 180°, respectively. Therefore, the carbon atoms in a hexagonal lattice could be substituted into CG beads in a triangular lattice, as shown in Figure 22d.

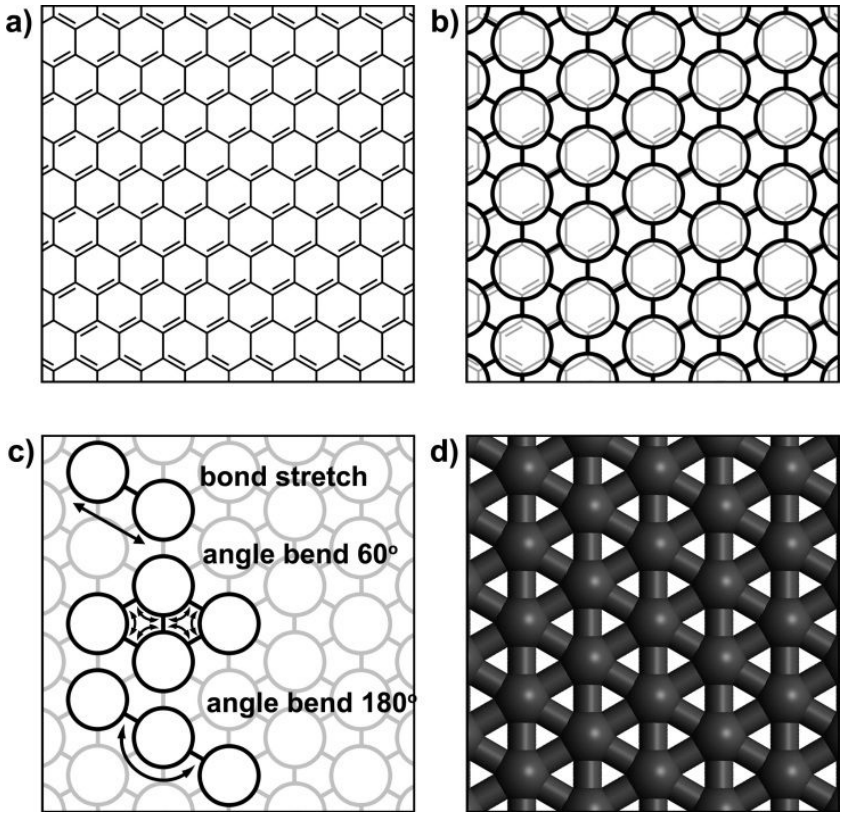

Figure 22. Schematic illustration of the formation of the CGNS for DPD simulation: a) molecular structure of the sp^2 hybridized graphene nanosheet and b) formation of the CG bead by grouping six neighboring carbon atoms with c) bond stretch and angle bend limitations. Each bead is linked to six adjacent beads in the CGNS by harmonic springs. Harmonic bend potentials for 60° and 180° angle are applied on the equilateral triangle geometry and the linear form from three neighboring beads, respectively. d) CG beads are shown with spheres by 3D representation.

In general, DPD simulation has been applied to predict the self-assembly phenomenon for soft materials of fluidic system. The value of spring constant k for bead connection is dependent to the bonding properties which may differ from the modeled system, but has usually been set as 4 in DPD unit for linear organic molecules or polymeric chain.[83,84] However, in the case of carbon nanomaterials, the spring constant k should be adjusted to reflect the rigidity of bonding between beads and mechanical properties of carbon nanomaterials.[85,86]

In order to calibrate the spring constant k, a CGNS with rectangular shape (about 6.8×5.9 nm^2) was modeled by 263 CG beads. It is important to introduce angle bend force constants between bonded beads as well as the spring constant, owing to the structural feature of the graphene nanosheet. Therefore, the angle bend constants for equilibrium angle of 60° and 180° were temporarily set as $40k_BT$/rad^2, which is rigid enough to hold two-dimensional structure of CGNS. The DPD simulations (NVT ensemble) were applied in a cubic simulation box filled water beads with a CGNS using periodic boundary condition in order to predict the equilibrium structure of the CGNS. At each spring constant k, 3.6 ns DPD simulation was performed with a time step of 0.02τ.

Figure 23 represents the dependence of the bond length between

neighboring CGNS beads and spring constant k. The average bond length can be calculated by the first peak position of radial distribution function (RDF) g(r), which represents the transition of the density distribution of the beads according to the distance from a reference bead. The g(r) is defined as,

$$g(r) = \frac{1}{4\pi r^2 \rho \ \mathrm{d}r} n(r) \tag{12}$$

where $n(r)$ is the number of beads at a distance between r and r + dr from a reference bead and ρ is the bead density. The bond length between CG beads decreases with increasing the spring constant k, which is caused by the strong stretch between the beads in Eq. (3) as shown in Figure 23.

In particular, the bond length at $k = 11k_BT/r_c^2$ reaches the theoretical value of 4.26 Å calculated from the theoretical bond length between carbon atoms in graphene structure (1.42 Å). However, when the constant k is above $20k_BT/r_c^2$ then the simulation results showed a failure with structural collapse of CGNS and extremely high temperature up to 1000 ^oC after time evolution, owing to the excessive bonding potential. Figure 24 represents the RDF value of the intra-CG beads with Gaussian fitting at $k = 11k_BT/r_c^2$. In the RDF results, the position of the first peak coincides with that of the g(r) of

theoretical triangular lattice having 4.26 Å distance between lattice points.

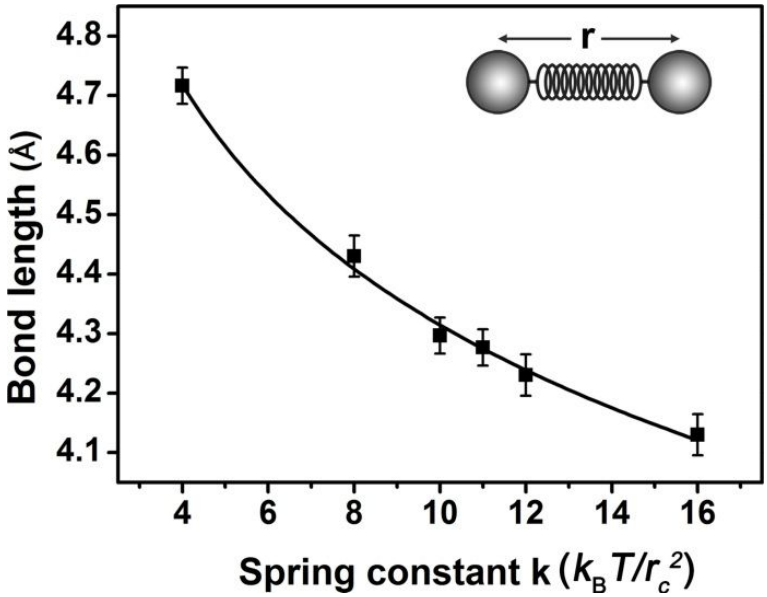

Figure 23. Bond length between neighboring two CG beads in the CGNS with the spring constant k.

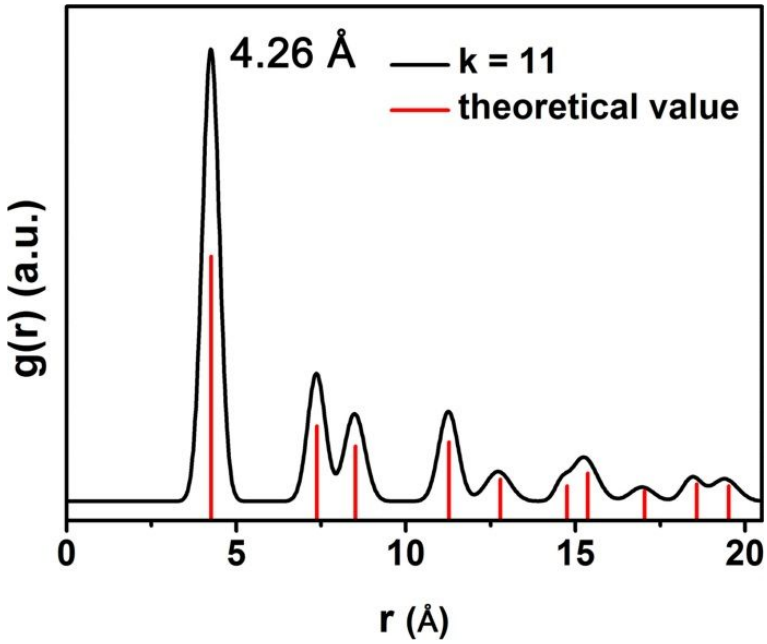

Figure 24. RDF value of the intra-CG beads according to the spring constant $k = 11k_BT/r_c^2$.

In the literature, coarse-grained metal nanoparticles for DPD simulation have been modeled by combination of harmonic springs in order to maintain their unique structure features.[87] Besides, angular forces were introduced to the coarse-grained modeling for CNT,[88] and angular force with dihedral angle force was set to CGNS by Martini force field.[62] In this study, two types of angular force were simultaneously applied to maintain the structural properties of graphene. The angle bend constants for the equilibrium angle of 60° and 180°, which were temporarily set as $40k_{B}T/\mathrm{rad}^{2}$, were calibrated by analyzing the equilibrium morphologies of the CGNS. The DPD simulation was carried out using equivalent condition with the calibration step.

Figure 25 demonstrates the equilibrium morphologies of the CGNS with angle bend constants after time evolution. The W beads are not shown for clarity. When the angle bend constants were both 0, indicating that the angular potential could not affect on the CGNS, the CGNS was collapsed like benzene molecules in water. It was hard to maintain the triangular lattice with two-dimensional structure without angular potential. For the constants $< 10k_{B}T/\mathrm{rad}^{2}$, the CGNSs represented the distortional surface with the bond-length distribution, while the CGNS had the two-dimensional properties. In the case of the constants $> 20k_{B}T/\mathrm{rad}^{2}$, it was found that the CGNS had

comparatively stable bond length distribution, except for the edge region because the CG beads of edge region had fewer number of bonding than that of basal plane region. The equilibrium structure of CGNS could reveal the rectangular shape with uniform bond length and the two-dimensional surface properties from side view, when the constants were above $30k_BT/\mathrm{rad}^2$. Judging from these results, the introduction of the angular potential was attributed to the two-dimensional and triangular lattice properties of the CGNS. And the angle bend constants $30k_BT/\mathrm{rad}^2$ or higher were needed for the maintenance of structural properties.

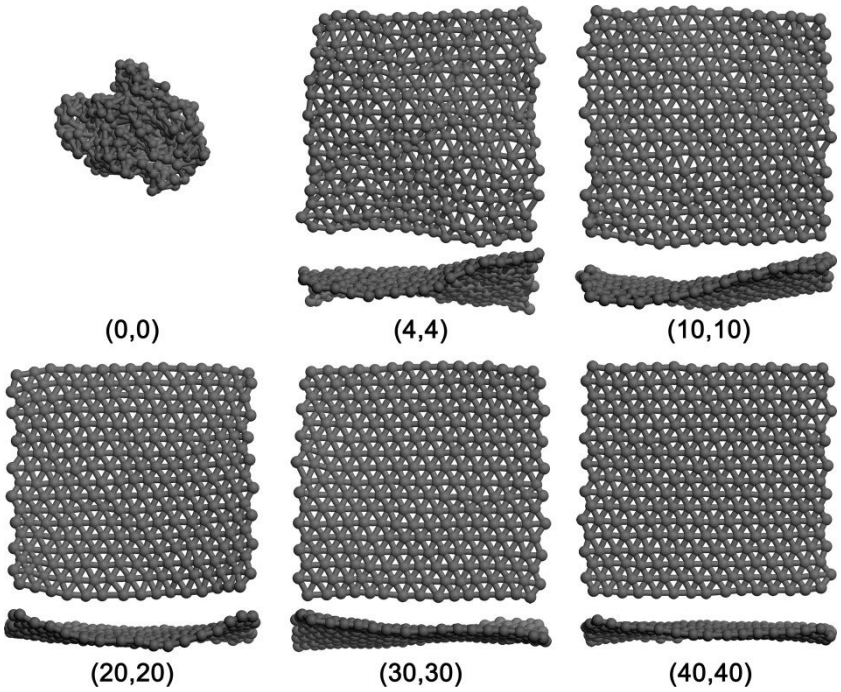

Figure 25. Equilibrium morphologies of the CGNSs with angle bend constants.

The contour plot for the RDF value of intra-CG bead is obtained for the calibration with increasing the angle bend constants of the CGNS by $4k_BT/\text{rad}^2$ as shown in Figure 26. The first peak of the RDF (4.26 Å), corresponding to the average bond length between CG beads, became broader and weaker with decreasing the angle bend constants. In particular, the first peak was much broader and weaker below $20k_BT/\text{rad}^2$, representing that the bond length distribution was not uniform. Moreover, the position of the first peak remained by changing the angle bend constants. This results that that the average bond length could be primarily dependent on the spring constant k. The angle bend constants were optimized at 36, since the RDF corresponded with theoretical value over above $32k_BT/\text{rad}^2$.

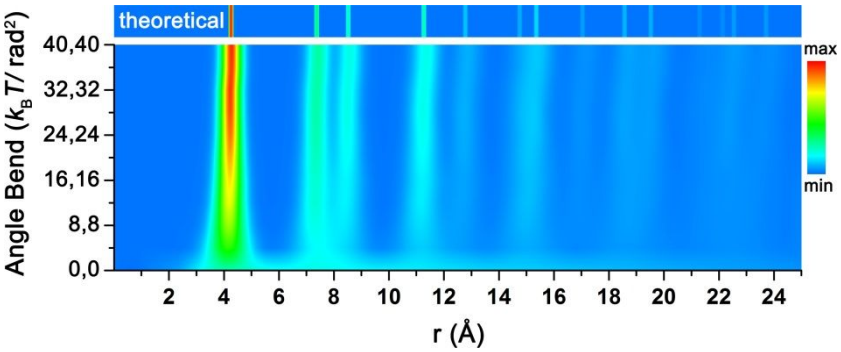

Figure 26. The contour plot of *g*(r) for the equilibrium morphologies with the angle bend constants.

To verify the proposed CSDS model, the micelle structure for single CSDS micelle (N = 66) was observed. A spherical CSDS micelle was obtained after 20 ns of DPD simulation, as shown in Figure 27a. The number density of bead T with radial distribution was decreased from 1.5 nm to 2.3 nm, indicating the alkyl radius of the micelle. And the maximum peak at 2 nm in bead H density represented the the radius of the micelle, as shown in Figure 27b. There was no bead W in the regions of the bead T. Judging from these results, the proposed CSDS molecule is good agreement with the results of all-atomic MD with Coulomb interaction [74,89] as well as the results of experiments from XRD.[90]

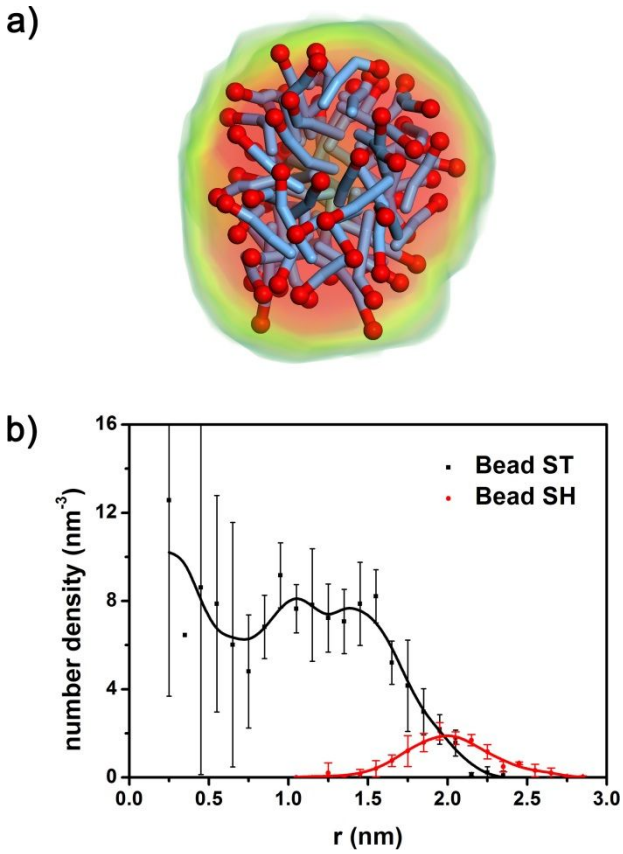

Figure 27. a) A spherical CSDS micelle at equilibrium phase with the density field of bead H and b) number density of beads from the center of a CSDS micelle.

3.2.2 Self-assembly phenomenon between graphene and surfactant by dissipative particle dynamics simulation

A rectangular CGNS with size of 8.09 × 8.11 nm^2 was introduced in the simulation box of $V_{box} = (30r_c)^3$ for the self-assembly phenomenon of graphene and surfactant. This simulation box was equivalent to about 23 × 23 × 23 nm^3 with 283 surfactant beads and water beads while periodic boundary condition was adopted all three directions. Coarse-grained sodium dodecyl sulfate (CSDS) as a surfactant was simply represented by single head (H) bead and three tail (T) beads.[59]

In Figure 28, it was investigated that the CSDS could be adsorbed onto the CGNS in aqueous solution with time step. At the establishment state of the DPD simulation, the CSDSs were randomly dispersed in the water beads and were adjusted to prevent the penetration into the CGNS. The CSDSs immediately started to agglomerate in the solution and to adsorb onto the CGNS because of the hydrophobicity of the CSDS. After t = 1.8 ns, there are spherical micelles formed by the CSDS and CGNS/CSDS adsorption structure in the simulation box. Judging from this simulation, it seems that the micelle collapses through the insertion of the CGNS and the residual CSDS by collapse adsorbs onto the CGNS surface, simultaneously. After ca.

40 ns, all CSDS in the periodic boundary adsorb onto the CGNS and form a hemispherical micellar structure with the CGNS.

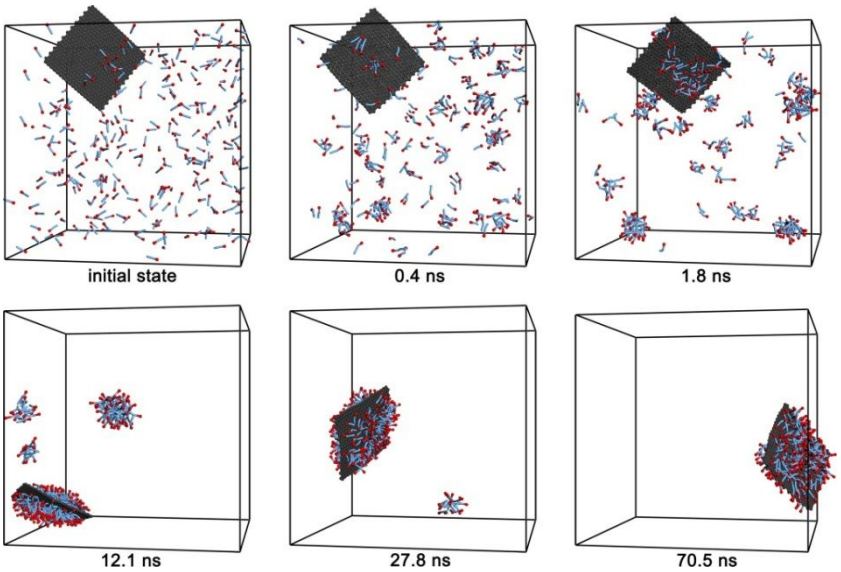

Figure 28. Dynamics of the CGNS and CSDS beads in aqueous solution from a random phase. The head groups of the CSDS and tail groups consisting of hydrocarbons are shown with red spheres and sky blue rods, respectively. Water beads representing fiver water molecules are not shown for clarity.

To further investigate the adsorption behavior of the CSDS, the time evolution of phase separation in the system was calculated by order parameter P_1,

$$P_1 = \frac{1}{V}\int [\eta_i^2(r) - \eta_i^2]\mathrm{d}r \tag{13}$$

where $\eta_i(r)$ is a dimensionless density for bead i. Order parameters with large values indicate that the system is strongly separated each other.[91] In Figure 29, the value of order parameter for the CGNS has changed little, indicating that the CGNS did not transform the conformation of the CG bead during the simulation. In the case of the T beads representing tail groups of CSDS, the order parameter rapidly increases until 10 ns, owing to the formation of the micellar structure and the adsorption onto the surface of CGNS. While the residual micelles collapse by the CGNS, the value of order parameter for T beads continuously increases. After about 40 ns, the P_1 reaches the equilibrium phase which ensures that the whole system achieve to the steady state.

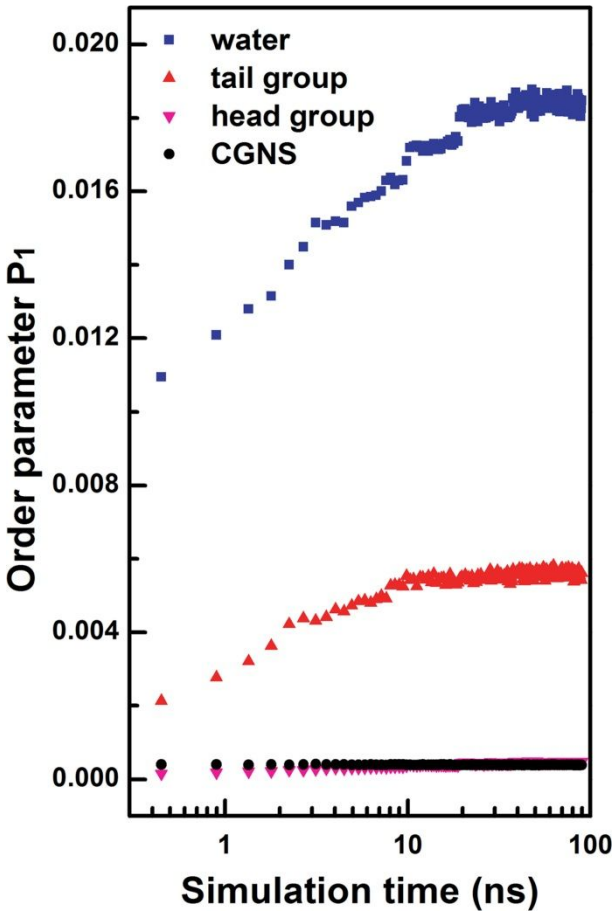

Figure 29. Order parameter P_1 of CG beads for the CGNS/CSDS solution.

The simulation results of the self-assembly between the CGNS and CSDS indicated that the CGNS could adsorb the CSDS micelles as well as the single CSDS molecule by the hydrophobic interaction between CG and T beads representing the benzene ring and hydrocarbon, respectively. In the micelle adsorption, the CGNS could lead to collapse of the micellar structure and adsorption of the CSDS onto the CGNS surface, simultaneously. To clarify this micelle collapse phenomenon by the CGNS, simulated collision experiments between the CGNS and the CSDS micelle were suggested. The collision was induced by moving the CGNS and the micelle with same initial velocities, but in opposite direction. The initial velocities were set to about 3 Å ps^{-1}, in order to assign an initial temperature which was similar to the simulation temperature. Initial velocity for the water beads were generated from the Gaussian distribution for random motion.

When the CGNS edge penetrated the center of CSDS micelle, the CSDSs collapsed by the collision and adsorbed onto both sides of the CGNS, as shown in Figure 30a. In the case of the contact with the basal plane, the CSDSs could adsorb only with the contacted surface. Judging from there results, the micelle collapse by contact with graphene edge would be more efficient than basal plane, owing to its drag force as well as the pentrating possibility.[92] Therefore, it can be considered that the micelle collapse and

adsorption phenomenon by the edge of graphene would be dominant in the initial state of self-assembly for graphene/surfactant micelle system.

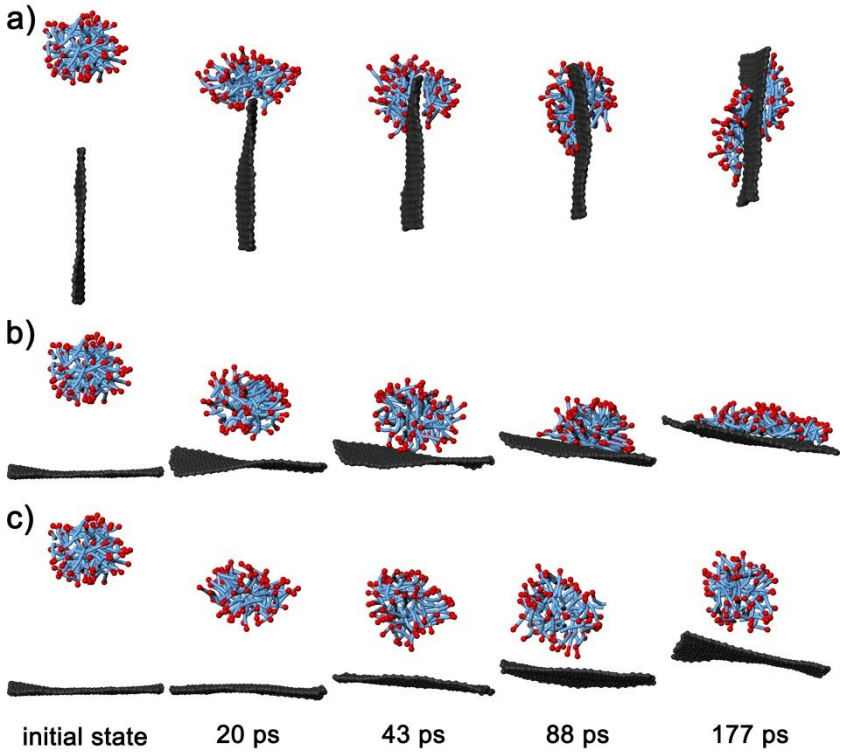

Figure 30. A collision simulation for a CSDS micelle with a CGNS. The micellar structure can be collapsed by a) the edge or b) the basal plane of the CGNS with an initial distance of 4 nm. c) In the case of 6 nm for the initial distance the collapse by the basal plane is not observed during the simulation.

Figure 31 shows the time to contact plot with the initial distance between the CGNS and the CSDS micelle. Immediately after the contact with the CGNS, the micelle started to collapse and adsorb on the surface of the CGNS. If the CGNS approached the micelle with the edge direction, the contact happened more quickly than that with the basal plane. In contrast, it took longer time for the direction of the basal plane to contact mutually. When the initial distance was above 5 nm, the micelle collapse was not observed, due to the difference in fluid resistance. As the CGNS moved with the edge direction, the reference area perpendicular to the direction of motion could be minimized; thus the drag effect was reduced.

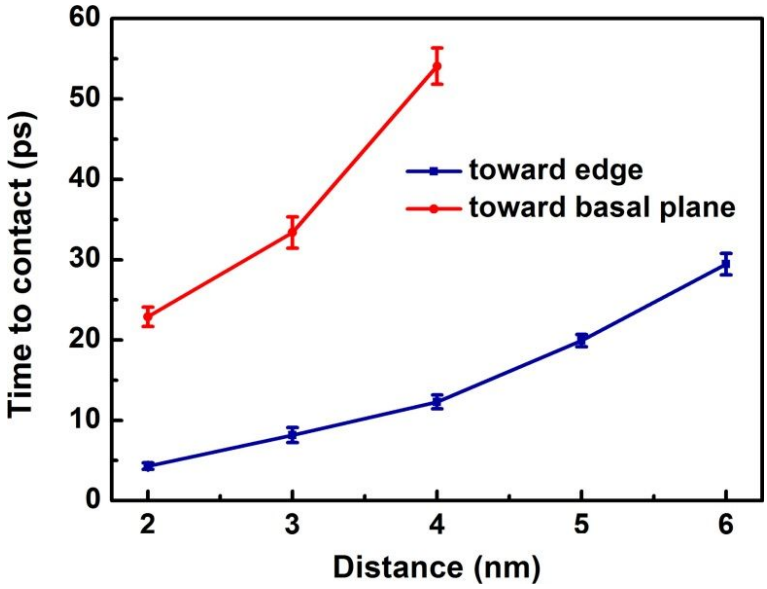

Figure 31. Time to contact plot with the distance between the CGNS and the CSDS micelle at initial state.

In the dispersion for carbon nanomaterials using ionic surfactants, hydrophobic sections of the surfactant are located onto the carbonaceous surface. And the hydrophilic groups situated in the exterior of the micellar structure make it possible to disperse the carbon nanomaterials in solution and prevent re-agglomeration.[57] Thus, DPD simulations for CGNS/CSDS were investigated with different CSDS concentrations in order to confirm the surface coverage effect. Each DPD simulation was conducted with random initial velocities from a temperature-dependent Gaussian distribution.

In Figure 32, the equilibrium structures of the CGNS with the number of CSDS are given with density fields for the T beads to improve the clarity of the surface coverage and the distribution onto the CGNS. When the number of CSDS (N_{CSDS}) = 143, the CSDSs could not provide adequate coverage on both sides of the CGNS in the equilibrium structure. The area of both sides of the CGNS per introduced surfactant was about 0.92 nm^2 per surfactant which is similar ratio to yield a monolayer structure on graphite.[35] However, in this study, CSDSs located near the edge of the CGNS were parallel arrangement of the plane, while hemispherical micellar structures were observed on the CGNS surface which was far from the edge. In addition, there was an asymmetric adsorption on the CGNS surface, since each side has different possibilities to contact with the CSDSs during the

dynamics.

The area occupied by the T beads was extended with higher concentration as shown in Figure 32. In all cases of concentration, the CSDSs on the CGNS edge were mainly arranged parallel to the plane and perpendicular to the edge, while the H beads pointed towards water beads and there were hemispherical structures at the central region of the CGNS. These equilibrium morphologies were caused by self-assembly to minimize the contact of the water with graphene and surfactant tail groups. Our results are in good agreement with those called 'lateral confinement effect' using all-atom MD simulation given by Naga *et al.*[63]

To further investigate the adsorbed structure at higher concentration, the concentration profiles of the T beads and H beads were calculated as a function of the distance perpendicular direction to the CGNS plane from each equilibrium structure. When the N_{CSDS} increase up to 0.06 M, the first peak at ~ 0.6 nm (the monolayer structure at the edge) and the second peak at ~ 1.2 nm (the hemispherical structure at the central region) increase in the T beads concentration profile. It indicates that the surface coverage of the CSDS surfactant is expanded by increasing the number of CSDS in monolayer and hemisphere structure onto the CGNS. This tendency is also observed in the H bead with different peak position. There is no significant

increase in the intensity of the first peak for T bead concentration profile at 0.08 M. Instead, a new peak is generated around the origin and the residual peak above ~ 1.2 nm increases as shown in Figure 33. It means that the additional CSDSs would be beside the edge of the CGNS (not on the edge) and be on the hemispherical structure in Figure 6a, because there are no more adsorption sites on the CGNS surface. The concentration profile for H bead also reflects the unique adsorption structure at high concentration with rapid increases around the origin and first peak. Therefore, it could be concluded that the CSDS surfactants are effectively adsorbed not only onto the surface but also beside the edge of CGNS around 0.08 M (~ 0.23 nm^2 per surfactant).

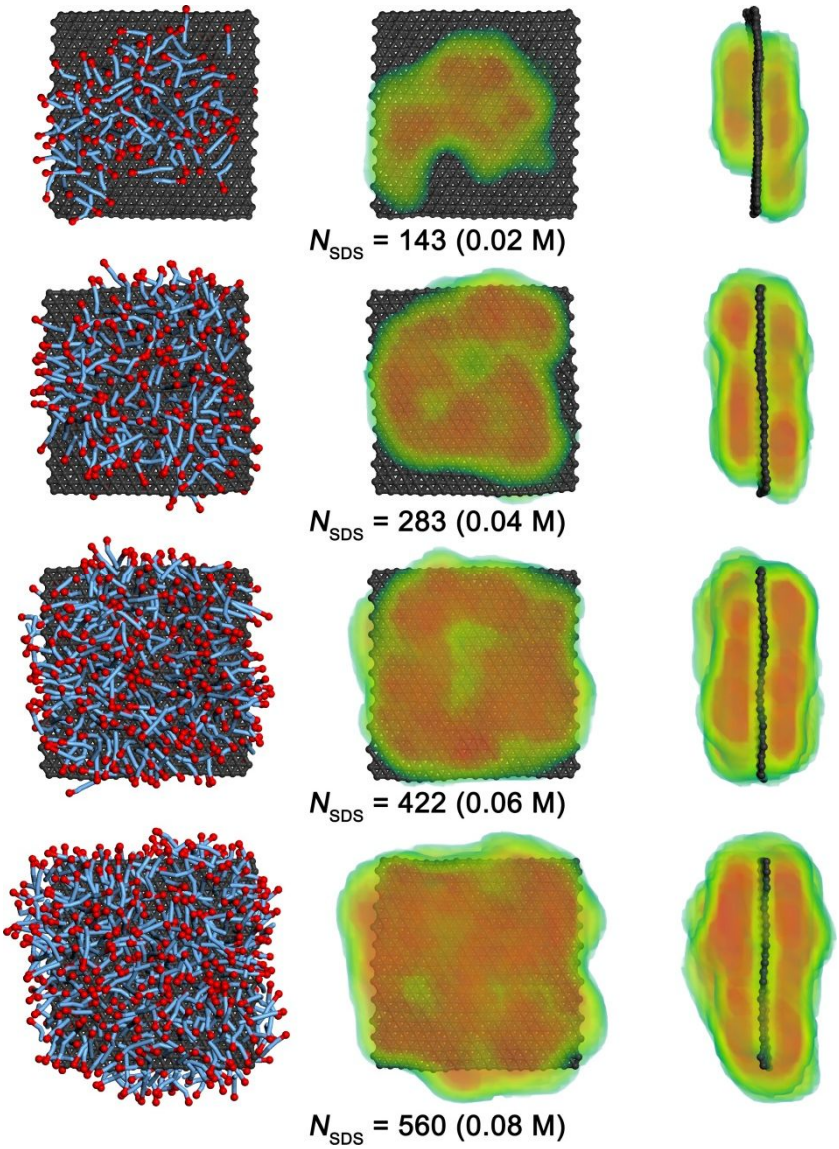

Figure 32. Micellar structure of CGNS/CSDS at equilibrium state with surfactant concentration

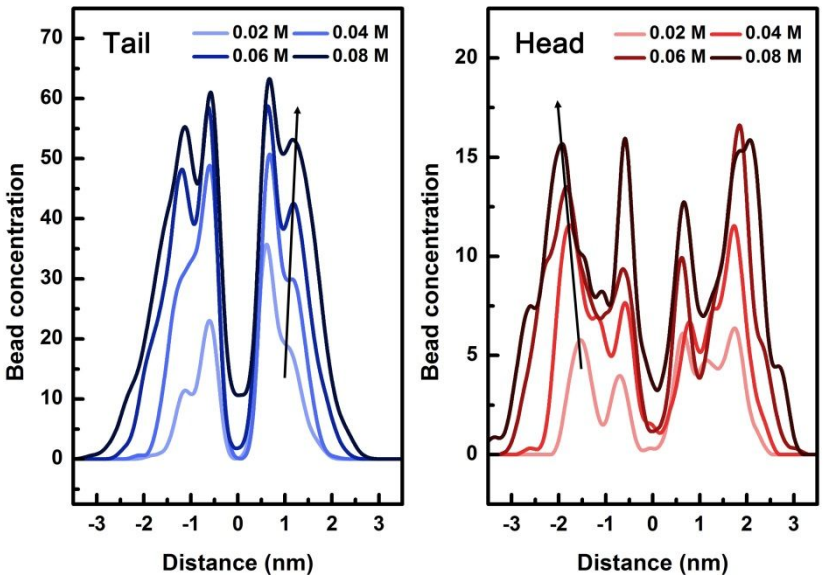

Figure 33. Bead concentration profile for the T and H beads of the CSDS.

3.3 CuO/graphene nanocomposite as an antimicrobial nanomaterial

3.3.1 Fabrication of CuO/graphene nanocomposite

The formation of the synthesized products is investigated using XRD peaks as shown in Figure 34. In XRD peak of the prepared GO, $2\theta = 10.5°$ belong to the (001) reflection of typical GO, which means large interlayer distance (~0.8 nm) due to inter-lamellar water trapped between graphene oxide sheets because of their hydrophilic hydroxyl, epoxy, and carboxyl groups. On the other hand, no distinct diffraction peaks of GO were observed in the rGO prepared in our experimental condition. The peak at $2\theta = 25°$ observed because the oxygen-containing functional groups are partially removed in the reduction process and the interlayer distance of rGO decreases.[93] In XRD peak of CuO/rGO composite, the diffraction peaks at ~ 35.6, 38.8, 48.8, 58.3, and 66.3° corresponds to the (-111), (111), (-202), (202), and (-311) planes are similar to these of CuO monoclinic phase (JCPDS 50-0661).[94] Additionally, the (001) peak of GO disappeared in CuO/graphene composite, which may indicate that the regular layered structure of GO has been destroyed and exfoliated due to the growth of CuO

nanocrystals.[95] The partial reduction of GO also can contribute to the disappearance of (001) peak.[93] Therefore, the XRD pattern demonstrates that CuO/rGO is successfully synthesized by the chemical reduction technique.

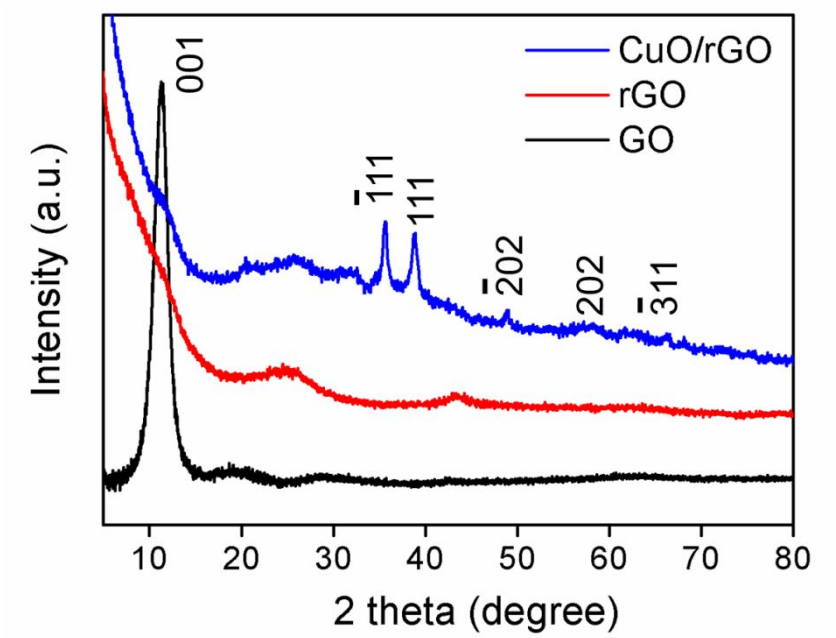

Figure 34. XRD patterns of the GO, rGO, and CuO-decorated rGO nanosheets. The characteristic peaks of CuO are indexed to CuO.

Raman spectra of GO and CuO/rGO composite are presented in Figure 35. In the Raman graphs, two prominent peaks of GO appearing at around 1343 and 1605 cm^{-1} are attributed to the D and G modes, respectively.[96] In the spectrum of CuO/rGO composite, the D and G modes of GO still exist. It is observed that the prepared nanostructure shows relatively higher intensity of D to G band (1.44) than that of GO nanosheet (1.16). These data confirm the formation of new graphitic domains after the metal oxide decoration process.[96]

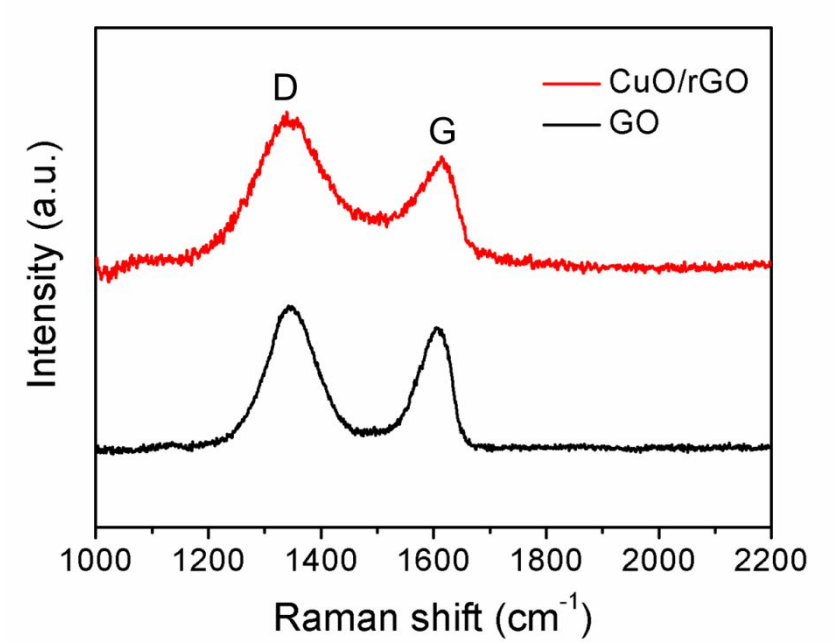

Figure 35. Raman spectra of GO and the CuO-decorated rGO nanosheet. The CuO/rGO obtained in presence of NH_4OH by hydrothermal treatment at 95 °C for 12 h.

Figure 36 exhibits the TEM and FE-SEM images of the synthesized CuO-decorated graphene oxide nanosheet. Interestingly, as a result of the chemical reduction synthesis, the formed CuO particles had urchin-like shape with average 150 nm in diameter. The highly magnified TEM (Figure 36b) and FE-SEM (Figure 36d) images further reveals that the urchin-like copper oxide consists of nano-needles; the average diameter and length of the nano-needles were approximately 10 nm and greater than 50 nm, respectively.

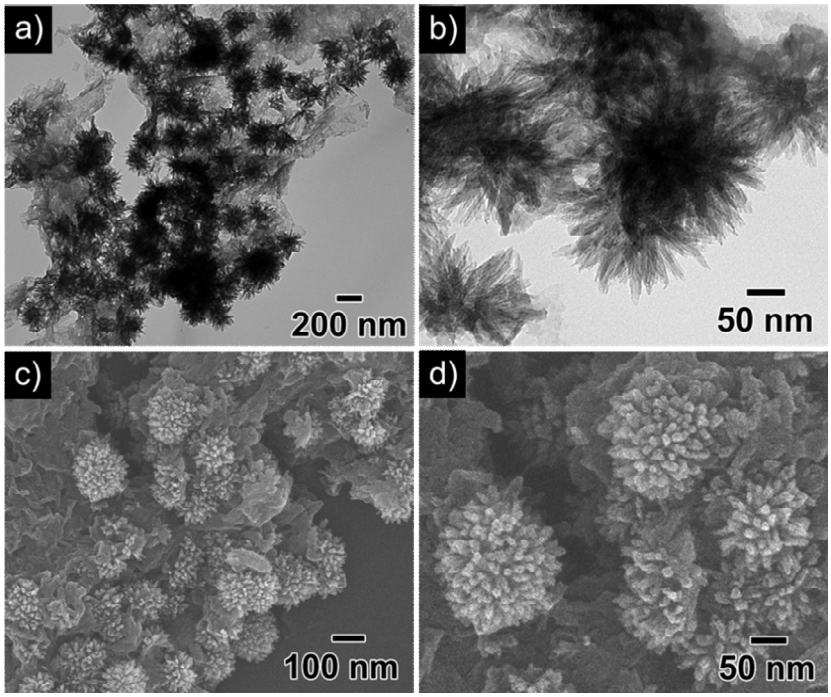

Figure 36. (a,b) TEM and (c,d) FE-SEM images of urchin like CuO-decorated rGO nanocomposites (left: Low-magnified images, right: high-magnified images).

In order to investigate the effects of GO nanosheet on the formation of CuO nanostructures, a comparative experiment was carried out. When the hydrothermal reaction was conducted without addition of graphene oxide with other experimental parameters being kept the same as in Figure 37, the product had plate-like morphology with several-tens micrometer scale (Figure 37a). These plates were composed of assembled 2-dimentional sharp plates with *ca.* 25 nm of thickness as shown in magnified FE-SEM image (Figure 37b). Based on the result, it can be suggested that the graphene oxide acts as a stabilizer for synthesis of urchin-like CuO nanostructure.

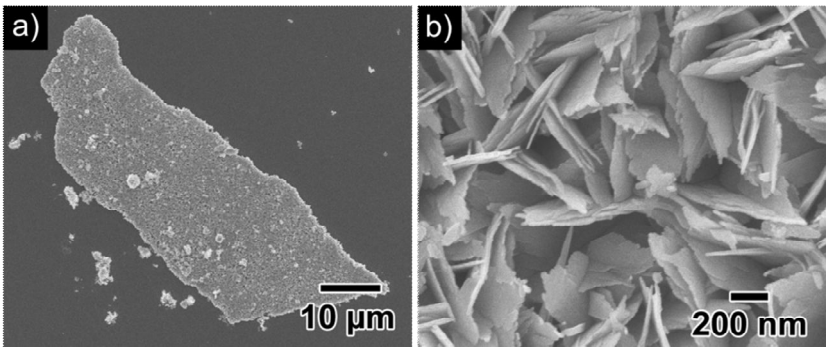

Figure 37. (a) Low- and (b) high-magnified FE-SEM images of copper(II) oxide prepared under the same condition as in Figure 3 except for the addition of GO solution.

When the GO solution introduced to the $Cu(OAc)_2$ solution, the Cu ions as a precursor of CuO adsorbed to GO *via* charge-charge interaction.[43] When the hydrothermal treatment started, the Cu-GO bonding would decompose and nucleate to form CuO nanocrystals. Then, the free GO sheet adsorb to the growing copper(II) oxide nanocrystals and inhibits the intrinsic anisotropic growth of CuO, resulting in the formation of assembled nanoplates. Through the further growth and crystallization process under hydrothermal conditions, the urchin-like CuO nanostructures were finally formed.

Typically, the $Cu(OAc)_2$ dissolved aqueous solution has green color. After introduction of ammonia solution, the solution dramatically turned to deep blue because the Cu^{2+} ion become ammonium complex, $[Cu(NH_3)_4]^{2+}$.[94] Then, the complex is hydrolyzed at 95 °C for 12 h and water-dispersible copper(II) oxide was obtained (Figure 38). The CuO is formed according to the following equation.

$$Cu^{2+}_{(aq)} + 4NH_4OH_{(aq)} \longrightarrow [Cu(NH_3)_4]^{2+}_{(aq)} + 4H_2O \qquad (14)$$

$$[Cu(NH_3)_4]^{2+}_{(aq)} + 2OH^-_{(aq)} + 4H_2O \longrightarrow Cu(OH)_{2(s)} + 4NH_4OH_{(aq)} \qquad (15)$$

$$Cu(OH)_{2(s)} \xrightarrow[\Delta]{} CuO_{(s)} + H_2O \qquad (16)$$

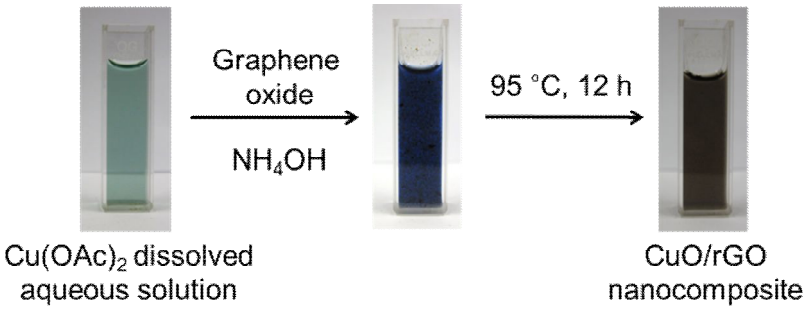

Figure 38. Typical photograph indicating the synthesis of CuO/rGO nanocomposite. The emeraldine $Cu(OAc)_2$ solution turned to deep-blue with adding of ammonia solution and it changed to gray color with hydrothermal reaction at 95 °C for 12 h.

To investigate the evolution process of the urchin-like CuO, time-dependent experiments were carried out, during which the samples were collected at different times after the heating was started. The samples were obtained at 4, 8, and 18 h, respectively. When the reaction time was 4 h (Figure 39b), the small nanoparticles (less than 10 nm) were formed on the surface of graphene nanosheet. As the reaction proceeded for 8 h, it was observed that the urchin-like copper(II) oxide nanoparticles with short and stubby needles. As shown in Figure 39e and 39f, these nanoparticles have *ca.* 100 nm of diameter. With the extension of the reaction time to 18 h, the size of the urchin-like CuO enlarged; the needles were elongated as the reaction proceeded. The formation of urchin-like copper(II) oxide was previously reported.[64,97,98] Xu et al. applied reflux method to prepare the urchin-like CuO. The copper(II) oxides strips were formed from copper nitrate hydroxide intermediate and aggregated as urchin-like structure.[64] Liu and Zeng prepared the urchin-like CuO nanostructures by hydrothermal process using copper nitrate as precursor. They suggested that the urchin-like morphology consisted of aggregation of strips which were readily formed within a short reaction time.[98] In our experimental condition, it was observed that the seeds were firstly formed and they grow to urchin-like morphology as the reaction proceeded. Time-dependent experiments

suggested that the urchin-like CuO nanostructures were grown from the seeds which were located on the graphene oxide surface. We believed that the graphene oxide acts as a template for the formation and growth of urchin-like CuO nanostructure.

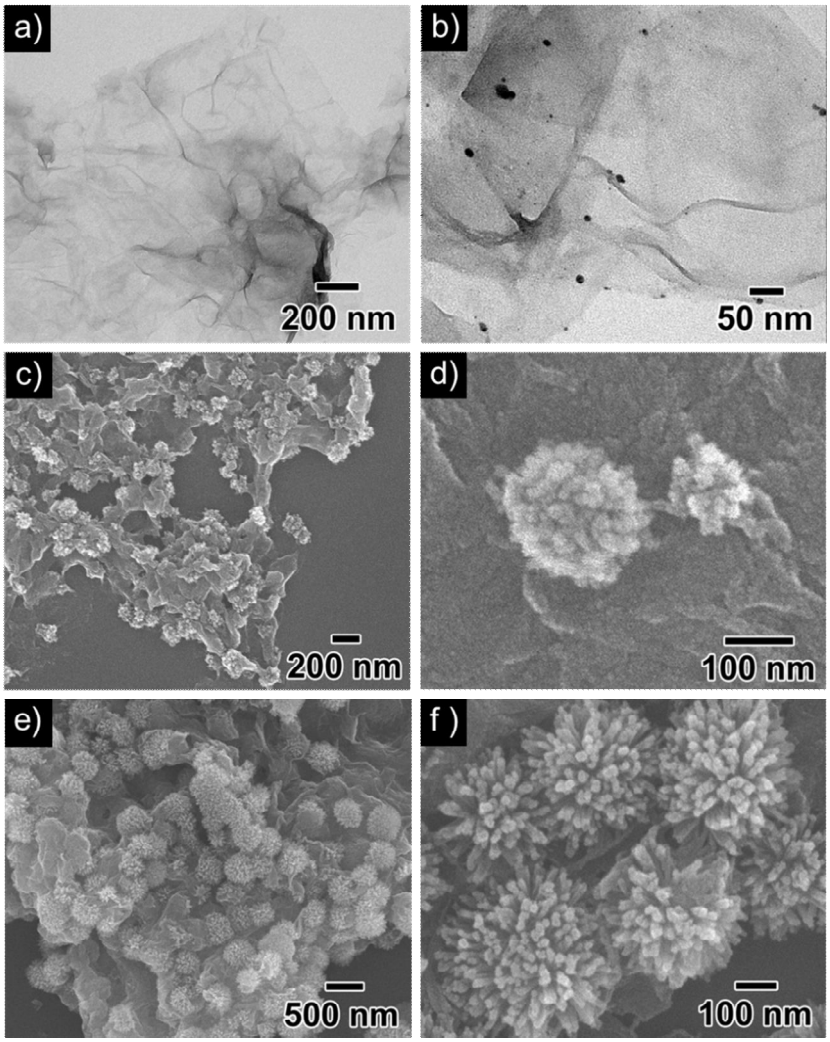

Figure 39. (a,b) TEM and (c-f) FE-SEM images of CuO/rGO nanocomposites prepared under the same condition as in Figure 3 except for different reaction times: (a) pristine GO, (b) 4, (c,d) 8, and (e,f) 18 hour.

Photocatalytic activity of the CuO/rGO nanocomposite has been investigated with degradation of dye molecules (methylene blue) under UV light irradiation (Figure 40). The CuO as p-type semiconductor acts as photocatalyst under UV-light irradiation. The aqueous solution of methylene blue exhibits a double-peak feature at 678 nm and at 625 nm, which correspond to monomers and dimers, respectively. The absorption peak of the solution continuously decreases as the photocatalytic reaction proceeds. Because the product from degradation of methylene blue has no light-absorption or emission feature in the scanned spectral region, the decrease of peak intensity indicated that the degradation of methylene blue molecule under UV illumination. Additionally, the rGO may be beneficial in the photocatalytic activity by reducing the recombination of photogenerated electrons and holes. Based on these data, the CuO/rGO nanocomposite can serves as photocatalysts to induce the decomposition of the pollutants.

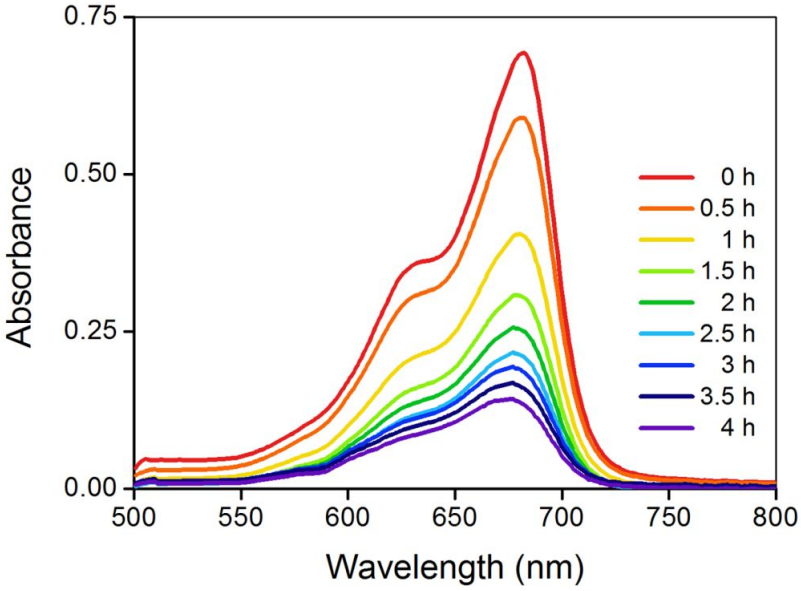

Figure 40. Absorption spectra of the methylene blue at different times since the photocatalytic reaction started under irradiation of UV light with assistance of the CuO/rGO nanocomposite.

3.3.2 Antimicrobial properties of CuO/graphene nanocomposite

The prepared urchin-like CuO nanoparticles onto rGO were expected to present antibacterial activities because the copper(II) oxide has bactericidal properties.[69,99,100] To evaluate the antibacterial activity of the as-prepared GO and rGO was prepared as comparative materials. A modified KB test was performed to investigate the antimicrobial abilities of the CuO/rGO nanocomposite (Figure 41). The distilled water-soaked filter paper (control), GO, and rGO-containing filter paper did not produce zones of inhibition when applied to either Gram-positive or Gram-negative bacteria. In contrast, filter papers containing CuO/rGO produced clear zones of inhibition when applied to the tested three of bacteria as shown in Figure 41. The observed zones of inhibition were attributed to the antimicrobial activity of copper ions and CuO released from the as-prepared nanocomposite. The copper oxide is known to release the copper ions which penetrate the cell wall and interact with RNA polymerase to exhibit efficient antibacterial properties.[99,100]

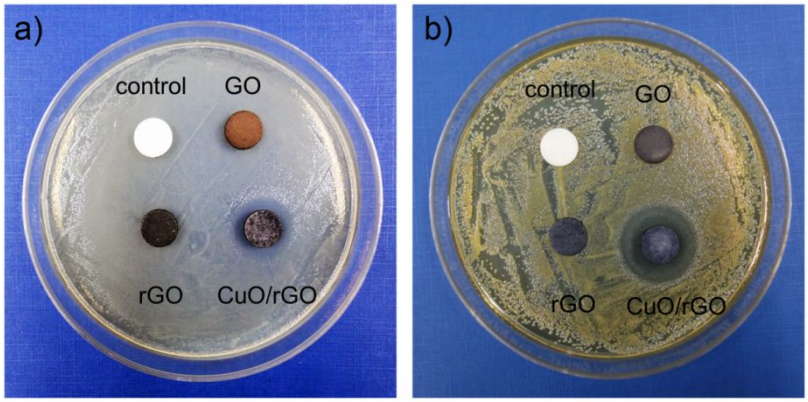

Figure 41. Photograph images of the zone of inhibition of prepared samples and control by the modified KB test against (a) *E. coli* and (b) *S. aureus*. The sample dispersed aqueous solutions were respectively dropped onto the filter paper and the filter papers were placed on the lawn of bacteria. Distilled water was used for the control. After 24 h of incubation at 37 °C, the zone of inhibition was observed. The filter paper sizes are 10 mm in diameter.

FE-SEM analysis was performed to further investigate the morphological changes in each bacterium after biocidal nanomaterial treatment. Intact *E. coli* had a rod-like shape (Figure 42a), whereas *S. aureus* were spherical shape (Figure 42c). After contact with the CuO/rGO nanocomposite, these bacteria had damage to their outer membrane and lost their cellular integrity (right row of Figure 42). These results suggest that the fabricated nanostructures have effective bactericidal properties.

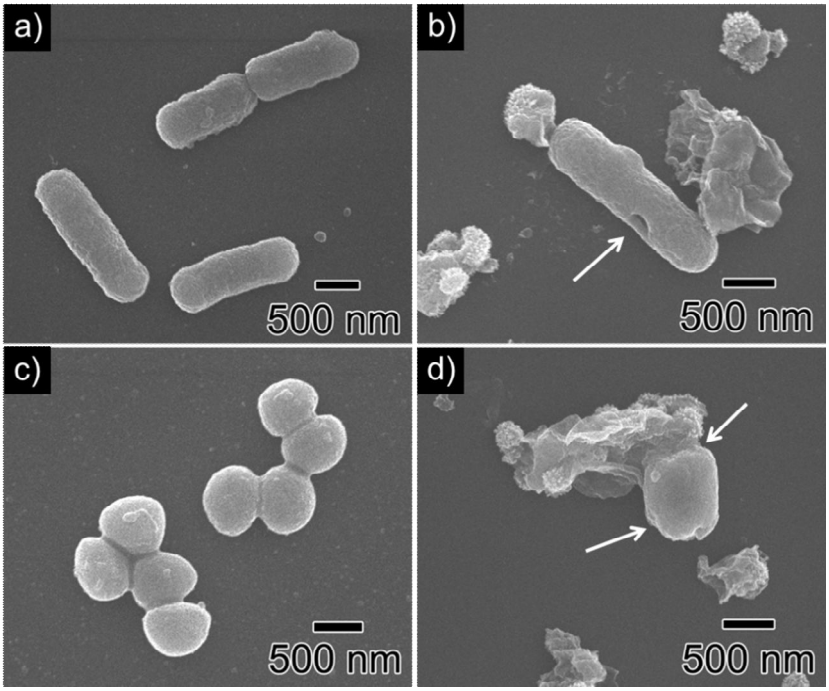

Figure 42. FE-SEM images of *E. coli* (top) and *S. aureus* (bottom) without being treated (a and c) and incubated with the CuO/rGO nanocomposites (b and d). The arrows in b and d indicate the damaged part of each bacterium.

For the kinetic antimicrobial test, the prepared samples (1 mg) were dispersed in aqueous solutions and they were inoculated with *E. coli* and *S. aureus* (10^5–10^6 CFU/mL). As a result, the densely grown bacterial colonies were observed on the LB agar inoculated with rGO nanosheet treated samples. In our experimental condition, the prepared rGO nanosheets did not show particular bactericidal performance against both Gram-positive and Gram-negative bacteria. On the other hand, the CuO-decorated rGO nanosheet has excellent bactericidal activity, with the contact time against the bacteria increasing based on the biocidal properties of the copper oxide. As shown in inset photographs of Figure 43, the CuO/rGO nanostructure killed over than 97 % of the tested bacteria (*E. coli* and *S. aureus*) within 30 min. The leached copper ions from the urchin-like CuO nanomaterials can interact directly with the bacterial membranes or be internalized to bacterium cell and disturb its metabolism, leading to the destruction of the membrane.[99,100] Based on this result, we conclude that the urchin-like CuO onto rGO nanosheet has excellent antibacterial performance against both Gram-positive and Gram-negative bacterial.

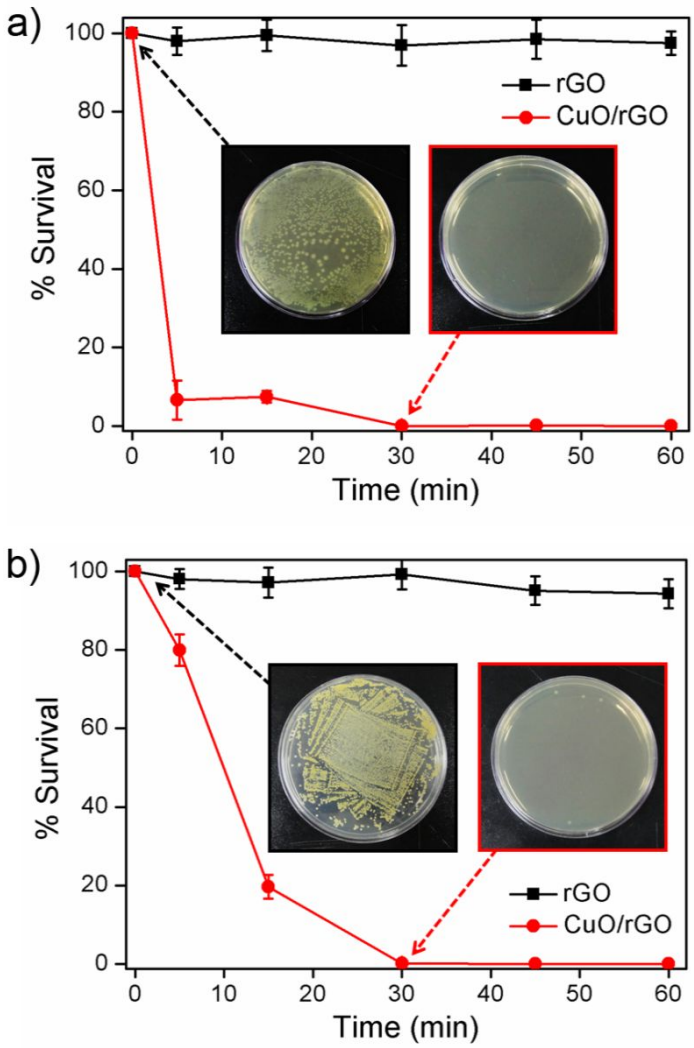

Figure 43. Antibacterial test graphs of the CuO/rGO nanocomposite (red circles) and rGO nanosheet (black boxes) as a function of contact time against (a) *E. coli* and (b) *S. aureus*. The insets show LB agar plates inoculated with bacteria at the corresponding conditions. The % survival was calculated as % survival = (A/B) × 100 (where A is the number of observed bacterial colonies of the test sample and B is that of the control).

3.4 Graphene-based nanofluid for enhancement of thermal conductivity

3.4.1 Fabrication of mechanical reduced graphene oxide using nanodispersion technique

The mechanical reduction of GO nanosheets was performed in the chamber of a T.K FILMICS mixer. First, the freeze-dried GO was re-dispersed in deionized water or EG by magnetic stirring and mild sonication. When the mixing occurred in the chamber, the rotation speed of the mixing blade immediately reached 54 m/s (indicating the 18400 rpm) and the temperature of the chamber reached 101 ^{o}C for water and 143 ^{o}C for EG within 30 seconds. The degree of reduction process was monitored by UV-Vis spectroscopy. Figure 44 shows the change of UV-Vis spectrum of mechanically reduced GO in water and EG. The maximum absorption wavelength of initial GO solution was 230 nm, which is related to π -π* electron transition in the polyene-type structure, as shown in Figure 44.

Judging from the cascaded bathochromic shift of λ_{max} and the hyperchromicity over the entire range (>230 nm), the electronic conjugation in GO structure could be gradually recovered after the mechanical mixing with high speed.

The mechanically reduced GO in water (rGO-water) and EG (rGO-EG) have maximum absorption wavelength at 264 and 275 nm, respectively. Considering these results of UV-Vis spectrum, the rGO-EG was exhibited high degree of reduction. There was little shift in maximum adsorption after 1 h, indicating completion of the reduction. These results suggest that the mechanical mixing can offer the possibility of controllable degree of reduction for GO solution by adjusting the mixing period, as well as the novel reduction method in mixing phase.

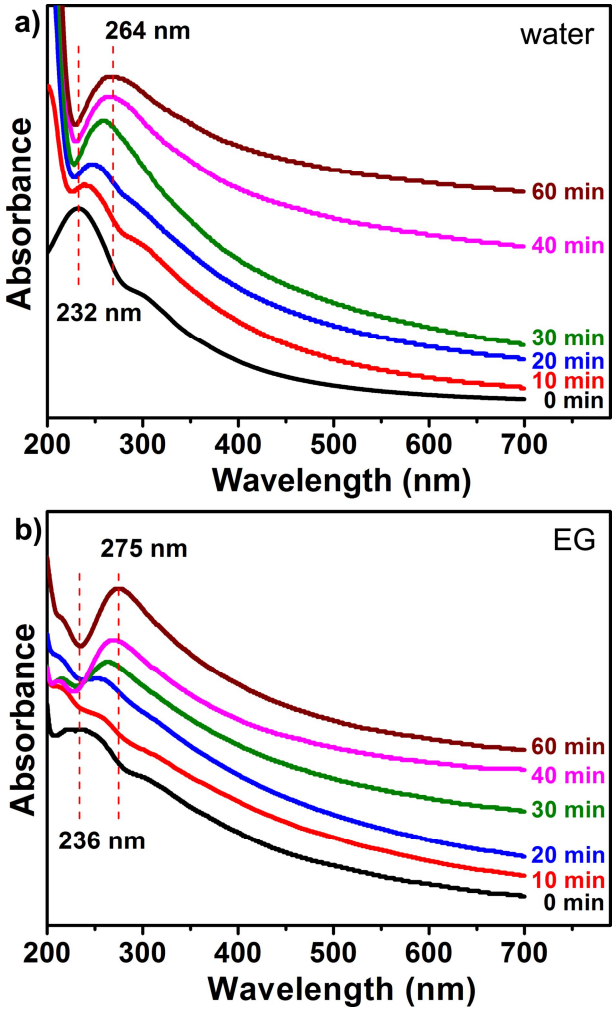

Figure 44. UV-Vis adsorption spectra of mechanically reduced GO solutions in a) water and b) EG with various mixing period.

The recovery of the original sp^2-hybridized structure of graphite by mechanical mixing was taken by XRD and Raman spectrum, as shown in Figure 45. The *d*-spacing of the freeze-dried rGO-water and rGO-EG was measured as about 3.66 Å and 3.56 Å, respectively. These *d*-spacing values are much lower than that of GO powder (7.12 Å), indicating that the GO solution could be reduced by mechanical reduction.

In Figure 45b, the Raman spectrum of the GO shows a typical peak of GO with the G band at 1597 cm^{-1} and the D band at 1334 cm^{-1}. After the reduction, the G bands of rGO became narrow and shift to 1591 cm^{-1}.

It has been known that the ratio of the D band to the G band (I_D/I_G) is related with the average size of sp^2-hybridized structure. The value of I_D/I_G increased from 0.99 to 1.3 and to 1.32, in the case of rGO-water and rGO-EG, respectively. Consequently, it can be considered that the mechanical mixing would offer a novel reduction route for GO solution by repairing defects. These results are comparable to the that of chemical reduction of GO,[70] and it implies that the graphene edge could increase after the break of GO nanosheet into smaller fragment during the mixing.

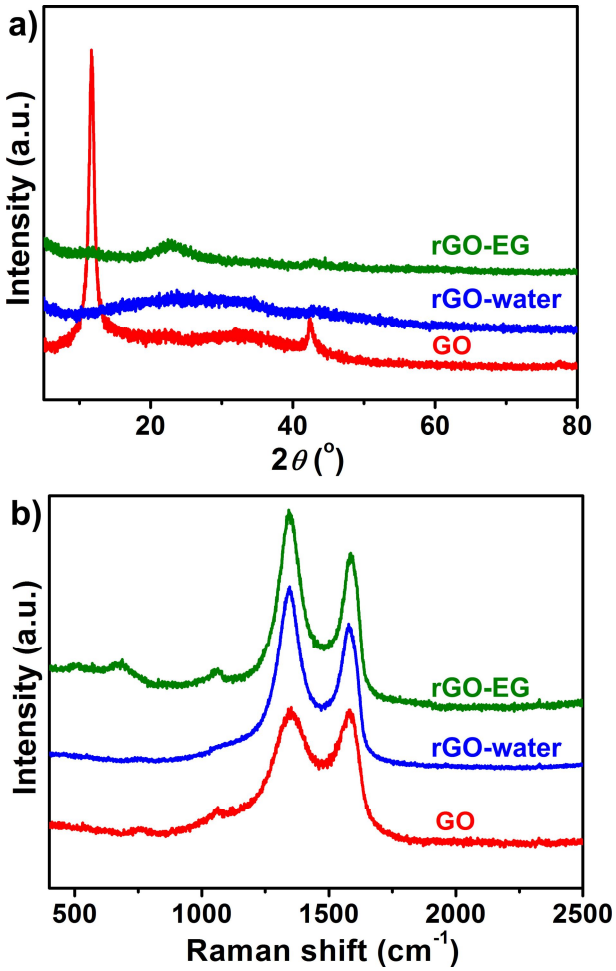

Figure 45. Structural properties of GO and rGO characterized by a) XRD, b) Raman analysis.

The removal of oxygen functional groups onto the GO was obtained with a ^{13}C NMR and XPS analysis. In Figure 46a, the NMR spectra of GO shows four peaks at 60, 70, 105 and 130 ppm, indicating the hydroxyl, epoxy, epoxide and conjugated double bonding groups, respectively.[101] After mechanical mixing with high speed, the two peaks related to oxygen functional groups at 60 and 70 ppm essentially disappeared, suggesting that the GO was successfully reduced by the mechanical mixing.

For further investigation of chemical bonding state after the mechanical mixing, XPS analysis was conducted. The XPS C1s and O1s spectra of GO samples were fitted by Gaussian function. In pristine GO, the peaks appeared at 286.4 eV and 288.5 eV for hydroxyl-epoxy and carbonyl group, respectively.[47] After reduction, these XPS peaks related to oxygen functional groups decreased, and the peak at 284.6 eV representing graphitic carbon increased from 45% to 71% and to 75% in the case of rGO-water and rGO-EG, respectively. The atom ratio of O:C was characterized using the elemental analysis to confirm the degree of reduction of GO. The ratio has changed from 0.45 to 0.16 (rGO-water) and 0.11 (rGO-EG) during the mechanical reduction. Judging from these results, the oxygen functional groups onto the GO surface could be removed by high-speed mechanical mixing.

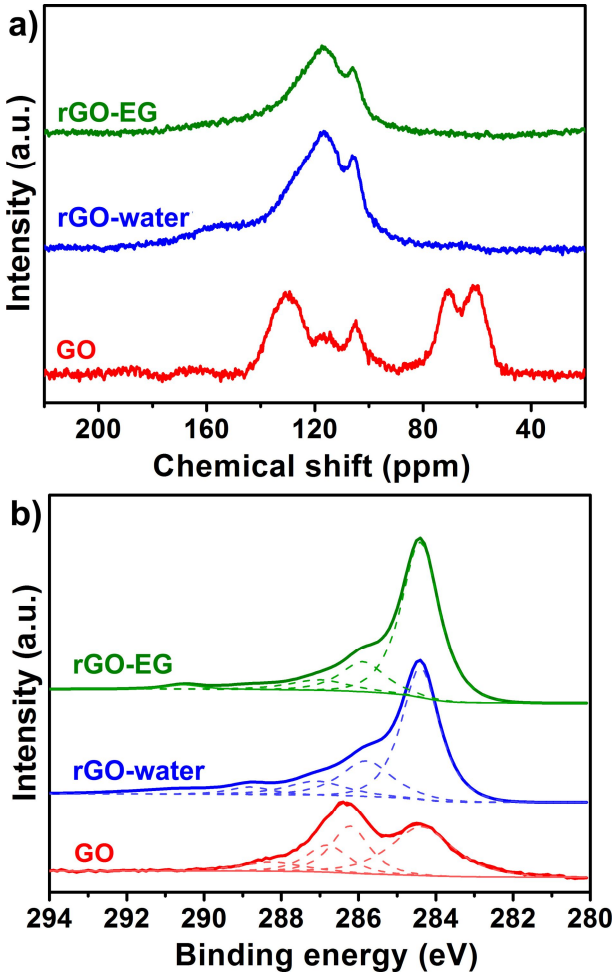

Figure 46. Structural properties of GO and rGO characterized by a) solid ^{13}C NMR and b) C1s XPS techniques.

It was difficult to achieve rGO with smooth surface by chemical reduction method, because plenty of defects, impurities and wrinkles would be remained on the surface of graphene nanosheets in process of chemical removal for oxygen functional groups.[102] However the TEM images of mechanical reduced GO demonstrates that the mechanical mixing provided the relatively smooth feature as shown in Figure 47. These reduced graphene nanosheets were also exhibited stable condition under the electron beam.

The smooth surface of the reduced GO should be an advantage for this mechanical reduction. Thin film along the wall of the mixer chamber would be formed by the high revolution speed of blade, and the thin-film spin methodology with high shear force would give a stress on the graphene sheet during the whole process of reduction. Another advantage is that the methodology of mechanical reduction is available for highly concentrated GO dispersion up to 10 g/L, showing the hydrogel-like behavior with high viscosity (~800 cP). In addition, the mechanical reduction can also be conducted with various solvents such as isopropanol and DMF, with superior stability.

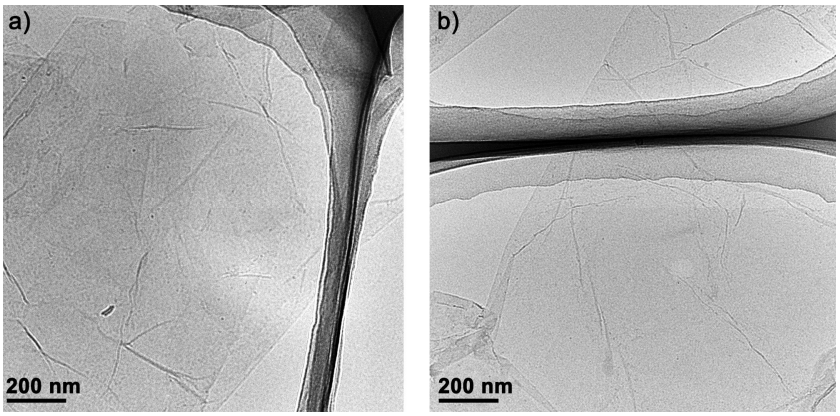

Figure 47. TEM images of a) rGO-water and b) rGO-EG.

3.4.2 Enhancement of thermal conductivity for the graphene-based nanofluid

It has been established that the ideal thermal conductivity of graphene monolayer is in the range 3,000 ~ 5,000 $Wm^{-1}K^{-1}$.[4] However, little studies have been reported to employ the graphene nanomaterials as a nanofiller of nanofluids. Therefore, it is expected that the mechanical reduced GO solution with high concentration and stability can be applied to the nanofluids for enhancement of TC.[103] The GO dispersion and rGO dispersion by mechanical reduction were fabricated for use as nanofluids.

Figure 48 shows a photograph of GO and rGO suspension in water and EG at 0.5 wt%. In any case, it showed dispersion stability about 1 month, indicating that the GO by mechanical reduction also had long-term stability in water and EG.

Figure 48. Photograph of GO and rGO suspension by mechanical mixing (0.5 wt%) after 1 months.

The enhancement of TC for these nanofluids were measured by the transient hot wire method.[104] Compared to steady-state method, this method makes measuring the thermal conductivity of fluids fast and accurate owing to measure it under stationary condition. The transient hot wire device has been verified by measuring the thermal conductivity of reference fluids (water and EG) at 25 ^{o}C.

Figure 49 shows the heat generated per unit length of Pt-wire and the temperature difference during the test experiments for reference fluids. The temperature of Pt-wire in the device increased linearly during the measurements as shown in Figure 49b. Thermal conductivity was calculated by Eq. (7) and shown in Table 3. The bias measurement error based on calibration with reference fluids such as water and EG, was within 1.5 %.

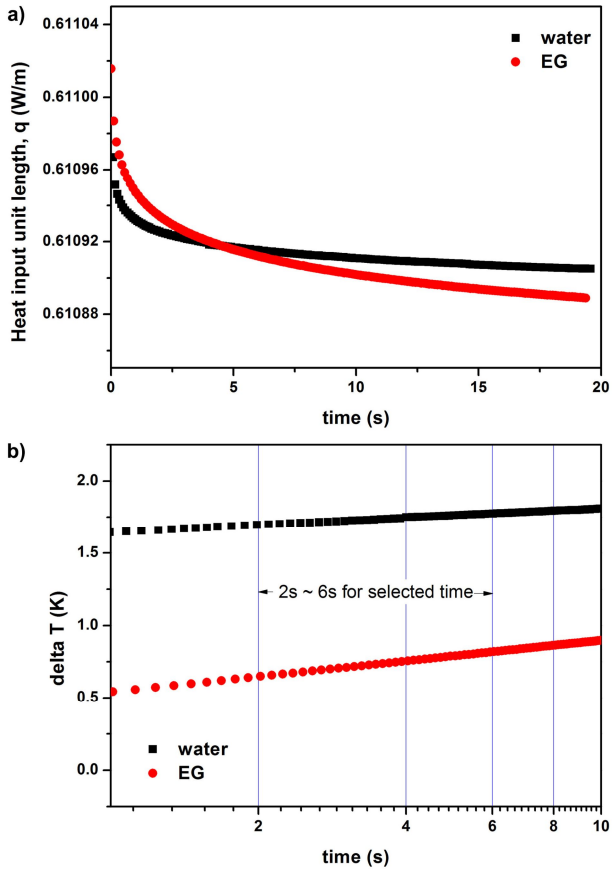

Figure 49. a) Heat per unit length of pt-wire and temperature difference during the measurement of thermal conductivity for reference fluids.

Table 3. Measurement of thermal conductivity for reference fluids.

Fluid	Reference (W/mK)	Measured (W/mK)	Bias error
EG	0.254	0.258	1.575%
Water	0.612	0.610	- 0.327%

The EG-based nanofluids were fabricated and TC enhancement was recorded as a function of concentration, as shown in Figure 50. The TC increased linearly with the concentration of GO nanofiller. After mixing with nanodispersion device (not exceeding the boiling point of EG), the TC had increased to about double. It was presumed that the GO sheets was well dispersed in the EG solution by wet-mixing technology. Additionally, the GO sheets in EG solution were reduced by mechanical mixing. In general, additional process *e.g.* surfactant or acid treatment was needed to produce well-dispersed rGO nanofluids.[104] However, stable rGO suspension could be obtained without any additional process by mechanical mixing technology. The TC of rGO-EG nanofluid have increased 17.4% compared to that of GO-EG nanofluid. The recovery of sp^2 carbon structure should contribute to the TC enhancement. Considering the significant TC enhancement, the graphene dispersions should be of a strong interest in the micro-scale liquid flow devices, which have compactness and high surface-to-volume ratio compared with conventional flow system.

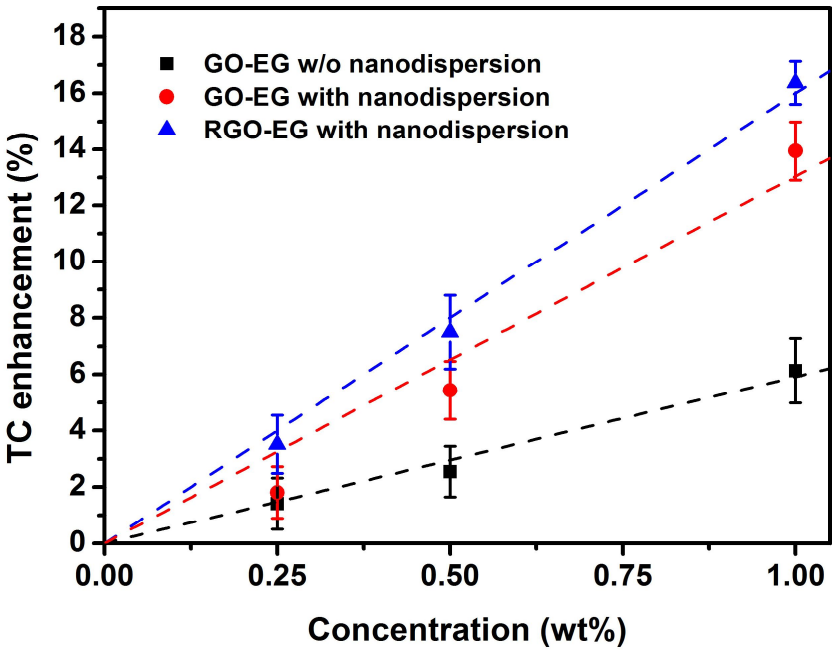

Figure 50. TC enhancement of EG-based nanofluids using GO, GO with nanodispersion and rGO with nanodispersion.

Chapter 4 Conclusions

The graphene nanomaterials was fabricated from graphite and applied to antimicrobial and nanofluid fields. Furthermore, graphene model for DPD simulation was proposed to prediction of self-assembly phenomenon between graphene and surfactants. The subtopics could be concluded as follows;

1. Novel type of rGO was successfully fabricated by exposing atmospheric-pressure argon plasma with freeze-dried oGO. The oGO could be reduced into oprGO, without any toxic chemical reducing agents. The oprGO was obtained above 140 W of RF power, in less than 10 seconds, and it was also observed that the oxygen functional groups in GO were successfully eliminated in XPS analysis.

Compared with previous reported studies on plasma-assisted reduction methods that need long exposure time and high vacuum condition, atmospheric plasma treatment to porous graphene oxide could be an alternative for mass production of rGO.

2. The coarse-grained graphene model has been successfully constructed by

adjusting the bond stretch and the angle bend constants. The adsorption dynamics of the SDS surfactant with the proposed graphene model composed of the 2D triangular lattice has been studied using dissipative particle dynamics. In the simulation results, graphene nanosheet could adsorb the surfactant micelles by collapse and adsorption phenomenon on impact, as well as a single surfactant molecule onto its surface. Owing to the edge effect, the surfactants lying on the edge of graphene are primarily in a parallel alignment with the basal plane and are perpendicular to the edge, while the surfactants located at the central region of graphene would form hemispherical micelle structures. At high ratio of the area of graphene surface to the number of surfactants, residual surfactants tend to be located beside the graphene edge, since there is no more space for adsorption on the surface.

It is expected that the proposed CGNS model could be used for simulation research areas such as self-assembly of graphene or graphene derivatives, surface functionalization of graphene and graphene/polymer nanocomposites by modifying some parameters.

3. Facile aqueous-phase chemical method was explored to synthesize copper(II) oxide nanostructures onto rGO nanosheet. The synthesized CuO

had an urchin-like shape densely composed of nano-needles. Through the time-dependent observation, it was confirmed that the copper(II) oxides grow from the seed particles located on the GO surface. It can be suggested that the GO nanosheet plays a role as stabilizer and template for the formation of copper(II) oxide nanostructure during the reaction. The synthesized nanocomposites presented excellent antibacterial performance against both Gram-positive (*E. coli*) and Gram-negative (*S. aureus*) bacteria. The urchin-like CuO/rGO nanostructure can be good candidate for various applications such as water-purification, pollutant removal, and inhibition of bacterial growth.

4. The GO solution was reduced by wet-mixing technique in solution phase. Owing to the enhanced sheer forces and dispersion effect, the GO solution showed high dispersion stability. This methodology may provide new possibility for the reduction of rGO without toxic reducing agent and the formation of rGO solution with long-term stability due to the mixing effect. Furthermore, the GO solution can be dispersed up to 10 g/L, and the obtained highly concentrated graphene dispersion in water and EG was applied as nanofluids for the enhancement of thermal conductivity.

These stable rGO dispersions without any reducing agents and surfactants

might be expanded to allow the large-scale applications such as flexible electronics, graphene-based nanocomposites and electrochemical devices.

In summary, the graphene nanomaterials was successfully fabricated from graphite and applied to antimicrobial and nanofluid fields. Atmospheric argon plasma treatment and mechanical mixing was also proposed to reduce the graphene oxide without toxic reducing agents. Furthermore, mesoscopic graphene model for DPD simulation was proposed to prediction of self-assembly behavior between graphene and surfactants. This study may provide novel approaches for reduction of graphene oxide and information for applications of graphene-based nanocomposite, as well as mesoscopic model of graphene nanosheet for coarse grained molecular dynamics.

References

[1] D. Li, R. B. Kaner, *Science* **2008**, *320*, 1170.

[2] C. Lee, X. Wei, J. W. Kysar, J. Hone, *Science* **2008**, *321*, 385

[3] K. I. Bolotin, K. J. Sikes, Z. Jiang, M. Klima, G. Klima, J. Hone, P. Kim, H. L. Stormer, *Solid State Commun.* **2008**, *146*, 351.

[4] A. A. Balandin, S. Ghosh, W. Bao, I. Calizo, D. Teweldebrhan, F. Miao,C. N. Lau, *Nano Lett.* **2008**, *8*, 902.

[5] Y. Choi, H. Bae, E. Seo, S. Jang, K. Park, B. Kim, *J. Mater. Chem.* **2011**, *21*, 15431.

[6] Y. Gao, D. Ma, C. Wang, J. Guan, X. Bao, *Chem. Commun*. **2011**, *47*, 2432.

[7] M. D. Stoller, S. Park, Y. Zhu, J. An,R. S. Ruoff, *Nano Lett.* **2008**, *8*, 3498.

[8] Y. Huang, J. Liang, Y. Chen, *Small* **2012**, *8*, 1805.

[9] P. Yang, S. Jin, Q. Xu, S. Yu, *Small* **2013**, *9*, 199.

[10] E. Kayhan, R. Prasad, A. Gurlo, O. Yilmazoglu, J. Engstler, E. Ionescu, S. Yoon, A. Weidenkaff, J. Schneider, *Chem. Eur. J.* **2012**, *18*, 14996.

[11] S. Pei, H. Cheng, *Carbon* **2012**, *50*, 3210.

[12] S. Park, R. Ruoff, *Nat. Nanotechnol.***2009**, *4*, 217

[13] M. Eizenberg, J. M. Blakely, *Surf. Sci.* **1970**, *82*, 228.

[14] T. Aizawa, R. Souda, S. Otani, Y. Ishizawa,C. Oshima, *Phys. Rev. Lett.* **1990**, *64*, 768.

[15] K. S. Novoselov, A. K. Geim, S. V. Morozov, D. Jiang, Y. Zhang, S. V. Dubonos, I. V. Grigorieva,A. A. Firsov, *Science* **2004**, *306*, 666.

[16] Z. Wang, X. Zhou, J. Zhang, F. Boey, H. Zhang, *J. Phys. Chem. C* **2009**, *113*, 14071.

[17] C. Berger, Z. Song, X. Li, X. Wu, N. Brown, C. Naud, D. Mayou, T. Li, J. Hass, A. N. Marchenkov, E. H. Conrad, P. N. First,W. A. de Heer, *Science* **2006**, *312*, 1191.

[18] K. S. Kim, Y. Zhao, H. Jang, S. Y. Lee, J. M. Kim, K. S. Kim, J. H. Ahn, P. Kim, J. Y. Choi,B. H. Hong, *Nature* **2009**, *457*, 706.

[19] P. Blake, E. Hill, A. Neto, K. Novoselov, D. Jiang, R. Yang, T. Booth, A. Geim, *Appl. Phys. Lett*. **2007**, 91, 063124.

[20] H. Wang, J. Robinson, X. Li, H. Dai, *J. Am. Chem. Soc.* **2009**, *131*, 9910.

[21] B. C. Brodie, *Ann. Chim. Phys.* **1860**, *59*, 466.

[22] L. Staudenmaier, *Ber. Deut. Chem. Ges.* **1898**, *31*, 1481.

[23] W. S. Hummers, R. E. Offeman, *J. Am. Chem. Soc.* **1958**, *80*, 1339.

[24] A. Lerf, H. He, M. Forster, J. Klinowski, *J. Phys. Chem. B* **1998**, *102*, 4477.

[25] G. Eda, M. Chhowalla, *Adv. Mater.* **2010**, *22*, 2392.

[26] P. J. Hoogerbrugge, J. M. V. A. Koelman, *Europhys. Lett.* **1992**, *19*, 155.

[27] P. Espanol, P. Warren, *Europhys. Lett.* **1995**, *30*, 191.

[28] P. Espanol, *Phys. Rev. E* **1995**, *52*, 1734.

[29] R. D. Groot, P. B. Warren, *J. Chem. Phys.* **1997**, *107*, 4423.

[30] R. D. Groot, K. L. Rabone, *Biophys. J.* **2001**, *81*, 725.

[31] C. M. Wijmans, B. Smit, R. D. Groot, *J. Chem. Phys.* **2001**, *114*, 7644.

[32] J. Shillcock, R. Lipowsky, *J. Phys.: Condens. Matter* **2006**, *18*, S1191.

[33] D. Krishnan, F. Kim, J. Luo, R. Cruz-Silva, L. Cote, H. Jang, J. Huang,

Nano Today **2012**, *7*, 137.

[34] I. Pivkin, B. Caswell, G. Karniadakisa, *Reviews in Computational Chemistry*, **2011**, *27*, 85

[35] N. Tummala, A. Striolo, *Phys. Rev.E* **2009**, 80, 021408.

[36] J. Wong-Ekkabut, S. Baoukina, W. Triampo, I. M. Tang, D. P. Tieleman,L. Monticelli, *Nat. Nanotechnol.* **2008**, *3*, 363.

[37] J. Song, H. Kong, J, Jang, *Chem. Commun*. **2009**, 5418.

[38] H. Zhou, C. Qiu, F. Yu, H. Yang, M. Chen, L. Hu, L. Sun, *J. Phys. Chem. C* **2011**, *115*, 11348.

[39] X. Liu, L. Li, C. Meng, Y. Han, *J. Phys. Chem. C* **2012**, *116*, 2710.

[40] L. Liu, H. Bai, Y. Wang, Z. Liu, X. Zhang, D. D. Sun, *Adv. Funct. Mater.* **2010**, *20*, 4175.

[41] Z. Wang, X. Zhan, Y. Wang, S. Muhammad, Y. Huang, J. He, *Nanoscale* **2012**, *4*, 2678.

[42] T. T. Baby, R. Sundara, *J. Phys. Chem. C* **2011**, *115*, 8527.

[43] H. Q. Xie, W. Yu, Y. Li, L. F. Chen, *Proc. ASME Micro/Nanoscale Heat Transf. Int. Conf.* **2009***,* 18445.

[44] C. Chon, K. Kihm, S. Lee, S. Choi, *Appl. Phys. Lett.* **2005**, *87*, 153107.

[45] V. Terekhov, S. Kalinina, V. Lemanov, *Thermophys. Aeromech*. **2010**, *17*, 1.

[46] S. Stankovich, D. A. Dikin, R. D. Piner, K. A. Kohlhaas, A. Kleinhammes, Y. Jia, Y. Wu, S. T. Nguyen, R. S. Ruoff, *Carbon* **2007**, *45*, 1558.

[47] W. Gao, L. B. Alemany, L. Ci, P. M. Ajayan, *Nature Chemistry* **2009**, *1*,

403.

[48] A. Ambrosi, C. K. Chua, A. Bonanni, M. Pumera, *Chem. Mater.* **2012**, *24*, 2292.

[49] M. J. Fernandez-Merino, L. Guardia, J. I. Paredes, S. Villar-Rodil, P. Solıs-Fernandez, A. Martınez-Alonso, J. M. D. Tascon, *J. Phys. Chem. C* **2010**, *114*, 6426.

[50] D. R. Dreyer, S. Park, C. W. Bielawski, R. S. Ruoff, *Chem. Soc. Rev.* **2010**, *39*, 228.

[51] M. Baraket, S. G. Walton, Z. Wei, E. H. Lock, J. T. Robinson, P. Sheehan, *Carbon*, **2010**, *48*, 3382.

[52] S. W. Lee, C. Mattevi, M. Chhowalla, R. M. Sankaran, *J. Phys. Chem. Lett*. **2012**, *3*, 772.

[53] M. Cardinali, L. Valentini, P. Fabbri, J. M. Kenny, C*hem. Phys. Lett.* **2011**, *508*, 285.

[54] M. Y. Kuo, H. C. Yang, C. Y. Hua, C. L. Chen, S. Z. Mao, F. Deng, H. H. Wang, Y. R. Du, *ChemPhysChem* **2004**, *5*, 575.

[55] J. Chanda, S. Bandyopadhyay, *J. Chem. Theory Comput.* **2005**, *1*, 963.

[56] P. Angelikopoulos, H. Bock, *J. Phys. Chem. B* **2008**, *112*, 13793.

[57] P. Angelikopoulos, A. Gromov, A. Leen, O. Nerushev, H. Bock, E. E. B. Campbell, *J. Phys. Chem. C* **2010**, *114*, 2.

[58] K. Yang, Y. Q. Ma, *Nat. Nanotechnol,* **2010**, *5*, 579.

[59] M. Calvaresi, M. Dallavalle, F. Zerbetto, *Small* **2009**, *5*, 2191.

[60] N. R. Tummala, B. H. Morrow, D. E. Resasco, A. Striolo, *ACS Nano* **2010**, *4*, 7193.

[61] R. Qiao, P. C. Ke, *J. Am. Chem. Soc.* **2006**, *128*, 13656.

[62] A. V. Titov, P. Král, R. Pearson, *ACS Nano,* **2010**, *4*, 229.

[63] N. R. Tummala, B. P. Grady, A. Striolo, *Phys. Chem. Chem. Phys,* **2010**, *12*, 13137.

[64] L. Xu, S. Sithambaram, Y. Zhang, C.-H. Chen, L. Jin, R. Joesten, S. L. Suib, *Chem. Mater.* **2009**, *21*, 1253.

[65] L. Rout, T. L. Sen, T. Punniyamurthy, *Angew. Chem. Int. Ed.* **2007**, *46*, 5583.

[66] R. Zou, Z. Zhang, L. Yu, Q. Tian, Z. Chen, J. Hu, *Chem. Eur. J.* **2011**, *17*, 13912.

[67] S. Jammi, S. Sakthyvel, L. Rout, T. Mukherjee, S. Mandal, R. Mitra, T. Punniyamurthy, *J. Org. Chem.* **2009**, *74*, 1971.

[68] B. Wang, X.-L. Wu, C.-Y. Shu, Y.-G. Guo, C.-R. Wang, *J. Mater. Chem.* ***2010**, 20,* 10661.

[69] G. Ren, D. Hu, E. W.C. Cheng, M. A. Vargas-Reus, P. Reip, R. P. Allaker, *Int. J. Antimicrob. Ag.* **2009**, *33*, 587.

[70] Z. H. Ni, H. M. Wang, Y. Ma, J. Kasim, Y. H. Wu, Z. X. Shen, *ACS Nano* **2008**, *2*, 1033.

[71] S. Guo, S. Dong, E. Wang, *ACS Nano* **2010**, *4*, 547.

[72] M. Calvaresi, M. Dallavalle, F. Zerbetto, *Small* **2009**, *5*, 2191.

[73] N. S. Martys, R. D. Mountain, *Phys. Rev. E* **1999**, *59*, 3733.

[74] W. Shinoda, R. Devane, M. L. Klein, *Soft Matter* **2011**, *7*, 6178.

[75] D. Li, M. B. Müller, S. Gilje, R. B. Kaner, G. G. Wallace, *Nature Nanotech.* **2008**, *3*, 101.

[76] L. Qian, E. Willneff, H. Zhang, *Chem. Commun.* **2009**, 3946.

[77] C. Korber, G. Rau, M. D. Cosman, E. G. Cravalho, *J. Cryst. Growth* **1985**, *72*, 649.

[78] S. G. Walton, C. Muratore, D. Leonhardt, R. F. Fernsler, D. D. Blackwell, R. A. Meger, *Surf. Coat. Technol.* **2004**, *186*, 40.

[79] S. Stankovich, D. A. Dikin, R. D. Piner, K. A. Kohlhaas, A. Kleinhammes, Y. Jia, Y. Wu, S. T. Nguyen, R. S. Ruoff, *Carbon* **2007**, *45*, 1558.

[80] H. Chen, M. B. Müller, K. J. Gilmore, G. G. Wallace, D. Li, *Adv. Mater.* **2008**, *20*, 3557.

[81] M. A. Worsley, P. J. Pauzauskie, T. Y. Olson, J. Biener, J. H. Satcher, T. F. Baumann, *J. Am. Chem. Soc.* **2010**, *132*, 14067.

[82] Y. Xu, K. Sheng, C. Li, G. Shi, *Acs Nano* **2010**, *4*, 4324.

[83] Z. Chen, X. Cheng, H. Cui, P. Cheng, H. Wang, *Colloids Surf., A* **2007**, *301*, 437.

[84] Y. Zhao, L. Y. You, Z. Y. Lu, C. C. Sun, *Polymer* **2009**, *50*, 5333.

[85] A. V. Titov, P. Král, R. Pearson, *ACS Nano* **2010**, *4*, 229.

[86] J. Wong-Ekkabut, S. Baoukina, W. Triampo, I. M. Tang, D. P. Tieleman, L. Monticelli, *Nat. Nanotechnol.* **2008**, *3*, 363.

[87] Y. L. Lin, C. S. Chiou, S. K. Kumar, J. J. Lin, Y. J. Sheng, H. K. Tsao, *J. Phys. Chem. C* **2011**, *115*, 5566.

[88] O. Liba, D. Kauzlaric, Z. R. Abrams, Y. Hanein, A. Greiner, J. G. Korvink, *Mol. Simul.* **2008**, *34*, 737.

[89] J. Gao, W. Ge, G. Hu, J. Li, *Langmuir* **2005**, *21*, 5223.

[90] R. Itri, L. Q. Amaral, *J. Phys. Chem.* **1991**, *95*, 423.

[91] M. Laradji, G. Hong, M. Grant, M. J. Zuckermann, *J. Phys.: Condens. Matter* **1992**, *4*, 6715

[92] K. Yang, Y. Q. Ma, *Nat. Nanotechnol,* **2010**, *5*, 579.

[93] Y. Gao, D. Ma, C. Wang, J. Guan, X. Bao, *Chem. Commun*. **2011**, *47*, 2432.

[94] N. Li, Z. Wang, K. Zhao, Z. Shi, S. Xu, Z. Gu, *J. Nanosci. Nanotechnol.* **2010**, *10*, 6690.

[95] J. Liu, L. Liu, H. Bai, Y. Wang, D. D. Sun, *Appl. Catal. B Environ*. **2011**, *106*, 76.

[96] S. Liu, J. Tian, L. Wang, Y. Luo, X. Sun, *Catal. Sci. Technol.* **2012**, *2*, 339.

[97] Z. Zhang, H. Che, Y. Wang, J. Gao, X. She, J. Sun, Z. Zhong, F. Su, *RSC Advances* **2012**, *2*, 2254.

[98] B. Liu, H. C. Zeng, *J. Am. Chem. Soc.* **2004**, *126*, 8124.

[99] C. Gunawan, W. Y. Teoh, C. P. Marquis, R. Amal, *ACS Nano* **2011**, *5*, 7214.

[100] S. Jadhav, S. Gaikwad, M. Nimse, A. Rajbhoj, *J. Clust. Sci.* **2011**, *22*, 121.

[101] H. He, T. Riedl, A. Lerf, J. Klinowski, *J. Phys. Chem.* **1996**, *100*, 19954.

[102] D.H. Long, W. Li, L.C. Ling, J. Miyawaki, I. Mochida, H.S. Yoon, *Langmuir* **2010**, *26*, 16096.

[103] L. Godson, B. Raja, D. Mohan Lal, S. Wongwises, *Renew. Sust. Energ. Rev.* **2010**, *14*, 629.

[104] K.J. Lee, S.H. Yoon, J. Jang, *Small* **2007**, *3*, 1209.

[105] W. Yu, H. Xie, W. Chen, *J. Appl. Phys.* **2010**, *107*, 094317.

[106] J. Bentley, *J. Phys. E* **1984**, 17, 430.

[107] S. Min, C. Lee, J. Jang, *Soft Matter* **2012**, 8, 8735.

초 록

화학적 박리에 의하여 흑연으로부터 그래핀 나노재료가 제조되었다. 특히, 산화 그래핀 용액을 동결주조 방법으로 처리한 결과, 섬유형태의 일차원적 산화그래핀이 제조되었고, 기상 환원반응을 통하여 형태 변화 없이 환원된 그래핀 산화물을 얻을 수 있었다. 또한, 제조된 섬유형태의 일차원적 산화그래핀에 아르곤 상압 플라즈마 처리시, 유독한 환원제 없이 10초 이내로 환원이 가능하였다.

그래핀 비드간에 추가적인 힘을 설정함을 통하여 소산입자역학 시뮬레이션을 위한 그래핀 모델이 제시되었으며, 구조분석을 통하여 보정되었다. 소산입자역학 방법을 이용하여 수용액 안에서 제안된 그래핀 모델과 계면활성제 간의 자기조립현상이 간접적으로 분석되었다. 계면활성제 분자뿐만 아니라 계면활성제가 이루는 마이셀과의 상호작용을 예측하였으며, 계면활성제 농도에 따라 다양한 그래핀/계면활성제 자기조립체 구조를 예측할 수 있었다.

박리된 산화그래핀을 이용하여 그래핀/산화구리 나노복합체를 액상에서 제조하였다. 나노 바늘모양으로 구성되어 있는 성게모양의 산화구리가 그래핀 표면에 도입되어있는 모양을 얻었으며, 이는 그람양성균과 그람음성균 모두에 대하여 뛰어난 항균 특성을

보였다. 또한, 높은 회전수를 통한 기계적 혼합기술을 이용하여 환원제 없이 산화그래핀 용액을 환원된 그래핀 산화물 용액으로 환원시켰다. 다양한 용매에 대하여 환원이 가능하였으며, 높은 분산 안정성을 보였다. 에틸렌글리콜을 기반으로 한 환원된 그래핀 산화물 용액을 나노유체로 적용하였으며, 1wt% 첨가 시 약 16.4%의 높은 열전도도의 향상이 있었다.

주요어: 그래핀; 플라즈마 환원; 소산입자역학; 항균; 나노유체
학 번: 2007-21187